Neurofibromatosis 1 *(NF1)* mutation results in impaired function of human induced pluripotent stem cell-derived microglia

Leonard D. Kuhrt[1,3,5], Edyta Motta[1,9], Nirmeen Elmadany[1,7,8], Hannah Weidling[1,5], Raphaela Fritsche-Guenther[2], Ibrahim E. Efe[1,5], Olivia Cobb[4], Jit Chatterjee[4], Lucy G. Boggs[4], Marina Schnauß[1], Sebastian Diecke[3], Marcus Semtner[1], Corina Anastasaki[4], David H. Gutmann[4,*], Helmut Kettenmann[1,6,*]

[1]Cellular Neurosciences, Max-Delbrück-Center for Molecular Medicine in the Helmholtz Association, Berlin, Germany
[2]Berlin Institute of Health (BIH) @ Charité – Universitätsmedizin Berlin, BIH Metabolomics Platform
[3]Technology Platform Pluripotent Stem Cells, Max-Delbrück-Center for Molecular Medicine in the Helmholtz Association, Berlin, Germany
[4]Department of Neurology, Washington University School of Medicine, St. Louis, Missouri 63110 USA
[5]Charité – Universitätsmedizin Berlin, Germany
[6]Shenzhen Institute of Advanced Technology, Chinese Academy of Sciences, Shenzhen, China
[7]German Cancer Consortium (DKTK), Clinical Cooperation Unit (CCU), Neuroimmunology and Brain Tumor Immunology, German Cancer Research Center (DKFZ), Heidelberg, Germany
[8]Department of Neurology, Medical Faculty Mannheim (MCTN), University of Heidelberg, Mannheim, Germany
[9]Department of Neurosurgery, University Medical Center Schleswig-Holstein, Kiel, Germany

[*]Address correspondence to:
Kettenmann, Helmut (kettenmann@mdc-berlin.de), ORCiD: 0000-0001-8208-0291
Gutmann, David (gutmannd@wustl.edu), ORCiD: 0000-0002-3127-5045

Keywords: microglia, Neurofibromatosis 1, human induced pluripotent stem cells, purinergic receptors, phagocytosis, motility

Abstract

Neurofibromatosis type 1 (NF1) is an autosomal dominant condition caused by germline mutations in the *NF1* gene. Children with NF1 are prone to the development of multiple nervous system abnormalities, including autism and brain tumors, which could reflect the effect of *NF1* mutation on microglia function. Using heterozygous *Nf1*-mutant mice, we previously demonstrated that impaired purinergic signaling underlies deficits in microglia process extension and phagocytosis *in situ*. To determine whether these abnormalities are also observed in human microglia in the setting of NF1, we leveraged an engineered isogenic series of human induced pluripotent stem cells to generate human microglia-like (hiMGL) cells heterozygous for three different NF1 patient-derived *NF1* gene mutations. While all *NF1*-mutant and isogenic control hiMGL cells expressed classical microglia markers and exhibited similar transcriptomes and cytokine/chemokine release profiles, only *NF1*-mutant hiMGL cells had defects in P2X receptor activation, phagocytosis and motility. Taken

together, heterozygous *NF1* mutation impairs a subset of human microglia functional properties, which could contribute to the neurological abnormalities seen in children with NF1.

Introduction

Microglia are specialized resident brain tissue macrophages that derive from the yolk sac and populate the developing central nervous system (CNS) during embryogenesis (Ginhoux et al., 2010; Hoeffel and Ginhoux, 2015). These brain monocytes constantly survey their local environment to ensure homeostasis, as well as change their functional phenotype in the setting of injury and disease. As such, microglia have been implicated as key regulators of neurodevelopmental, neuro-oncologic and neurodegenerative disorders, including autism (Derecki et al., 2012; Kana et al., 2019), brain cancer (Hambardzumyan et al., 2016; Pasqualini et al., 2020), and Alzheimer's dementia (Hong et al., 2016; Leyns et al., 2019). For the most part, their critical roles in human CNS disease have largely been explored in murine model systems using pharmacological and genetic approaches (Costa et al., 2021; Hammond et al., 2019; Sierra et al., 2019; Wolf et al., 2017). However, there are notable differences between murine and human microglia (Geirsdottir et al., 2020; Marsh et al., 2022), prompting the development of protocols to generate human microglia (Jairaman et al., 2022; McQuade and Blurton-Jones, 2022; Takata et al., 2017).

With further refinement of the methodologies to produce hiPSC microglia-like cells (hiMGL cells), it became possible to define the impact of disease-causing mutations on human microglia function. This is particularly important for neurodevelopmental and cancer predisposition syndromes, like Neurofibromatosis type 1 (NF1), where we have shown that heterozygous *Nf1*-mutant murine microglia have key contributions to low-grade brain tumor (glioma) pathogenesis (de Andrade Costa et al., 2022; Pan et al., 2018; Toonen et al., 2017; Solga et al., 2015a). To directly explore the impact of *Nf1* mutation on microglia, we previously identified sex-specific defects in microglia from mice heterozygous for a germline inactivating mutation in the murine *Nf1* gene (*Nf1*+/- mice) (Elmadany et al., 2020b). In this study, we found that male, but not female, *Nf1*+/- mice harbor microglia with impaired purinergic function, including reduced phagocytosis, microglia process extension, and ATP-induced membrane currents *in vivo*.

These intriguing findings suggested that *NF1* mutation might alter cell-intrinsic properties of microglia. To determine whether these *NF1* mutational effects were similarly observed in human male microglia in the setting of NF1, we leveraged an allelic series of CRISPR/Cas9-engineered male BJFF.6 hiPSCs harboring three different heterozygous NF1 patient-derived *NF1* germline mutations. In this report, we demonstrate that heterozygous *NF1* mutation in human hiMGL cells recapitulates some, but not all, of the purinergic defects observed in their murine counterparts. These findings

establish a foundation for future studies aimed at defining the cell-autonomous impact of germline mutations on human microglia function.

Results

NF1-*mutant human induced pluripotent stem cell-derived microglia-like (hiMGL) cells are phenotypically similar to isogenic control hiMGL cells*

Using a previously published protocol (McQuade et al. 2018), we generated hiMGL cells from male control BJFF.6 (CTL) hiPSCs that had undergone CRISPR/Cas9 engineering without creating a *NF1* gene mutation (**Fig. 1A**). Briefly, hiPSCs were seeded at low density and hematopoiesis initiated using the StemCell Technologies STEMdiff™ Hematopoietic Kit. Floating hematopoietic progenitor cells (HPCs) were harvested and reseeded in Geltrex™-coated 6-well plates on day 12 post induction (dpi). Microglial differentiation was induced under serum-free conditions by the addition of human M-CSF, human IL-34 and human TGF-β1, prior to supplementation with human CD200 and human CX3CL1 for an additional 3 days. Throughout the course of microglial differentiation, cells developed ramifications and started to adhere to the wells by 38 days in vitro (**Fig. 1A**).

To validate their microglial identity, we assessed *AIF1, TMEM119 and P2RY12* mRNA expression in the CTL lines at three different stages (hiPSCs, HPCs, hiMGL cells). For comparison, we analyzed the expression of these markers in human THP-1 macrophages (THP1 MΦ) and U87 human glioma cells (**Fig. 1B**). As expected for microglia-like cells, the expression of all three genes was increased in hiMGL cells compared to HPCs, while it was undetectable or expressed at very low levels in iPSCs, THP1 MΦ, and U87 glioma cells. Immunocytochemical staining of these hiMGL cells confirmed the expression of IBA1, TMEM119, and P2RY12 at the protein level (**Fig. 1C**).

To generate hiMGL cells harboring *NF1* gene mutations, we used previously published hiPSC lines in which three different NF1 patient-derived germline *NF1* gene mutations were heterozygously introduced into BJFF.6 hiPSCs by CRISPR-Cas9 editing: c.1149C>A; p.Cys383X **(M1)**, c.2041C>T; p.Arg681X **(M2),** and c.3431-32_dupGT; p.Thr1145Val_FS **(M3)** (**Fig. 2A**) (Anastasaki et al., 2020). These mutations were chosen because they create different brain tumor phenotypes in *Nf1* genetically engineered mice: Despite the fact that all generate premature termination mutations (two stop codons and one frameshift mutation) and increased RAS activity, the Cys383X mutation (Guo et al., 2019) results in lower optic glioma penetrance, while the Arg681X exhibits greater proliferation (Toonen et al., 2016), than the Thr1145Val_FS mutation (unpublished results). Moreover, we focused only on male hiPSC lines, in light of our prior discovery of male-specific deficits in murine *Nf1*-mutant microglia.

Pluripotency and genomic integrity were confirmed (**Fig. S1**) prior to hiMGL cell differentiation. *AIF1*, *TMEM119* and *P2RY12* transcript expression (**Fig. 2B**), as well as IBA1, TMEM119, and P2RY12 protein expression (**Fig. 2C** and **Fig. S2A**) by *NF1*-mutant hiMGL cells were indistinguishable from isogenic CTL hiMGL cells. We also assessed *TREM2* expression in CTL and *NF1*-mutant hiMGL cell lines and found no differences in mRNA levels (**Fig. S2B**). In addition, we examined signaling pathway activity in *NF1*-mutant hiMGL cells. Since our prior studies on *Nf1*-mutant murine microglia revealed that JNK, but not MAPK, activation was increased relative to their wild type counterparts (Daginakatte et al., 2008), we analyzed JNK phosphorylation, and observed increased activated (phospho-) JNK immunostaining in the *NF1*-mutant hiMGL cells relative to their CTL hiMGL counterparts (**Fig. S4**).

Transcriptome analysis reveals marked similarities between CTL and NF1*-mutant hiMGL cells*

To determine whether *NF1* mutation dramatically affected human microglia gene expression, we generated a minimum of three independent cultures from CTL and *NF1*-mutant hiMGL cells (M1 and M3) for bulk RNA sequencing analysis. Unfortunately, M2 *NF1*-mutant hiMGL cells could not be included in the analysis, as the resulting RNA failed quality control. While *NF1*-mutant hiMGL cells were distinct from CTL hiMGL cells by both principal component analysis (**Fig. 3A**) and hierarchical clustering (heat map; **Fig. 3B**), there were few differences between the two *NF1*-mutant hiMGL cell groups (0.047%; **Fig. 3C**) and only a modest number of differentially expressed genes between *NF1*-mutant and CTL hiMGL cells (0.044%; **Fig. 3D**) using a 5-fold cutoff. Gene ontology (KEGG) and gene set enrichment analysis (GSEA) revealed no differentially represented pathways or biological functions between *NF1*-mutant hiMGL cells relative to their CTL counterparts (FDR<0.25). Moreover, no significant differences in pathway or biological function enrichment were observed using either 2-fold or 3-fold cutoffs (**Fig. S3**).

Secretome analysis reveals marked similarities between CTL and NF1*-mutant hiMGL cells*

Given the paucity of transcriptomal differences, we next analyzed the ability of *NF1*-mutant hiMGL cells to release inflammatory paracrine factors in response to Lipopolysaccharide (LPS; 1 μg/ml) activation of the Toll-like receptor 4 (TLR4). TLR4 activation was chosen, as LPS is a commonly used agent to stimulate microglia function. *TLR4* RNA expression was similar in CTL and *NF1*-mutant hiMGL cells (**Fig. 3E**). Secreted IL-6 and TNF-α (**Fig. 3F**), as well as G-CSF, IL-1β, GRO, IL-10, IP-10, MCP-1, MCP-3, MIP-1β, MIP-1α, and CCL5 (RANTES) (**Fig. S5**), were similar in *NF1*-mutant and CTL hiMGL cells following 1 μg/ml LPS stimulation for 24h.

P2RY-dependent microglial membrane currents are similar in CTL and mutant hiMGL cells

Since the RNAseq and secretome analyses did not reveal any significant differences, we next focused on purinergic abnormalities previously reported in male *Nf1+/-* mouse microglia (Elmadany et al.,

2020b). Microglia express a variety of purinergic receptors, including members of the metabotropic P2Y and ionotropic P2X receptor families. To determine whether *NF1*-mutant hiMGL cells express known P2Y and P2X receptors, we leveraged our RNA sequencing data (**Fig. 3**). While M1 and M3 *NF1*-mutant hiMGL cells expressed similar levels of these receptors, we observed increased *P2RY4* RNA expression in the two *NF1*-mutants relative to their CTL counterparts (**Fig. S7B**).

First, we compared the membrane properties of microglia derived from CTL and *NF1*-mutant hiMGL cells. CTL hiMGL cells displayed microglia-characteristic membrane currents when repetitively clamped at potentials between -170 and +60 mV starting from a holding potential of -70 mV, similar to what we previously reported for mouse microglia (Elmadany et al., 2020b, 2020a; Kettenmann et al., 2011; Logiacco et al., 2023; Boucsein et al., 2000) (**Fig. S6A, B**). These cells were characterized by a high input resistance and a small inwardly rectifying potassium conductance between -40 and -170 mV. Similar relationships were seen in *NF1*-mutant hiMGL cells (**Fig. S6B**). There were also no differences in reversal potentials (CTL: -21.0 ± 2.3 mV, n = 38; M1: -25.0 ± 4.0 mV, n = 17; M2: -23.7 ± 3.9 mV, n = 18; M3: -20.8 ± 2.0 mV, n = 20; **Fig. S6C**), and the apparent membrane capacitances were indistinguishable from controls (CTL: 19.2 ± 1.4 pF; M1: 20.7 ± 2.2 pF; M2: 19.1 ± 1.3 pF, n = 18; M3: -16.6 ± 1.6 pF; **Fig. S6D**).

To identify potential P2Y- and P2X-based deficits, we then examined P2RY12 responses using standard whole-cell patch clamp techniques in the voltage-clamp configuration (**Fig. 4**), based on our previous report that murine male *Nf1*+/- microglia had defects in P2RY12 activation (Elmadany et al., 2020b). Consistent with these previous studies, CTL hiMGL cells responded to 10 µM ATP with the induction of outwardly rectifying currents that reversed close to the equilibrium potential for potassium (**Fig. 4A**). We determined the specific conductance to compare these currents in CTL and *NF1*-mutant hiMGL cells should be between +20 mV and +60 mV (**Fig. 4B**). Both CTL and *NF1*-mutant hiMGL cells exhibited similar conductances (CTL: 44.8 ± 12.5 pS/pF; n = 15; M1: 47.4 ± 11.7 pS/pF, n = 11; M2: 46.3 ± 7.2 pS/pF, n = 13; M3: 44.2 ± 11.8 pS/pF, n = 13) (**Fig. 4C, D**). These findings contrast with what we observed in *Nf1*-mutant murine microglia (Elmadany et al., 2020b). In addition, unlike *Nf1*+/- mouse microglia (Elmadany et al., 2020b), *NF1*-mutant hiMGL cells exhibited no differences in cAMP levels relative to controls (**Fig. 4E**).

P2X-dependent purinergic membrane currents are reduced in NF1*-mutant hiMGL cells*

Given the lack of differences in P2Y function, we next analyzed P2X receptor-mediated responses. Microglia membrane currents were measured following the application of 1 mM ATP (**Fig. 5**), a concentration sufficient to activate P2RX4 and P2RX7, the most common P2X receptor isoforms in microglia (Butovsky et al., 2014; Ousingsawat et al., 2015). In CTL hiMGL cells, the application of 1 mM ATP slowly induced membrane currents within the application period (60 s), which were

characterized by an inward and outward component and a reversal potential close to 0 mV, consistent with the characteristics of a non-selective cation channel (**Fig. 5A**). The specific conductance at -120 mV was 25.7 ± 6.2 pS/pF (n = 13) for CTL hiMGL cells (**Fig. 5B**). In contrast, 1 mM ATP did not evoke P2X-like ion currents in *NF1*-mutant hiMGL cells. Responses to 1 mM ATP were outwardly rectifying and had a reversal potential close to the Nernst potential for K^+, appearing similar to the responses seen following 10 µM ATP stimulation (**Fig. 5C**). This result suggests that *NF1*-mutant hiMGL cells have defective P2X receptor expression or function. While *NF1*-mutant hiMGL cells had similar levels of *P2RX4* and *P2RX7* RNA expression as CTL hiMGL cells (**Fig. S7A**), quantification of inward conductance as a measure of P2X-like currents revealed reduced conductances for M1 (3.5 ± 4.0 pS/pF, n = 9; p = 0.0024), M2 (0.2 ± 2.7 pS/pF, n = 14; p < 0.0001) and M3 (7.7 ± 1.0 pS/pF, n = 11 p = 0.0095) *NF1*-mutant hiMGL cells relative to their CTL counterparts (**Fig. 5D**).

Baseline motility is reduced in NF1*-mutant hiMGL cells*

In order to assay other microglia functions, we tested hiMGL cell motility in a wound-healing scratch assay using an Incucyte® Zoom Live Cell Imaging system with images automatically acquired every 4 hours. The Relative Wound Density (RWD) was calculated using Incucyte® Zoom software for each time point recorded, where the RWD was plotted against time (**Fig. 6A**). Interestingly, treatment of CTL hiMGL cells with 10 µM ATP did not affect the number of cells in the scratched zone, indicating that ATP at that low concentration was not sufficient to alter cellular movements. On the other hand, higher concentrations of ATP (1000 µM) led to faster wound healing, which was almost complete after 4h (RWD: 81.7 ± 45.7%), and therefore significantly larger than that observed under basal conditions without ATP (26.5 ± 4.9%; p = 0.0006).

We next investigated the impact of *NF1* mutation on hiMGL cell motility and found that *NF1*-mutant hiMGL cells had ~30% reduced baseline motility relative to their CTL counterparts 4h after generating the scratch (**Fig. 6B**, left). Exposure to 1000 µM ATP led to increased wound healing in CTL, M1, M2 and M3 hiMGL cells; however, the RWD observed in the M2 and M3 experiments was smaller compared to the CTL hiMGL cells. Likewise, after 24h under basal conditions, only M1 hiMGL cells produced an increase in RWD comparable to CTL hiMGL cells, whereas the RWD for the M2 and M3 hiMGL cells was smaller (**Fig. 6B**, right). Treatment of hiMGL cells with 1000 µM ATP led to a RWD increase to ~75-80% for both CTL and *NF1*-mutant hiMGL cells after 24h. Taken together, these data indicate that motility of hiMGL cells is reduced under basal conditions in an *NF1* mutation-dependent fashion.

Finally, we tested for the impact of the P2RY12, P2RX4 and P2RX7 purinergic receptors on ATP (1000 µM)-induced motility of CTL and *NF1*-mutant hiMGL cells, and compared the RWD of each

hiMGL cell line in the presence of 1000 µM ATP alone or together with either ARC-69931 (10 µM; P2RY12 inhibitor), 5-BDBD (100 µM; P2RX4 inhibitor) or A740003 (100 µM; P2RX7 inhibitor) (**Fig. 6C**). Interestingly, P2RY12 inhibition led to a reduction in initial wound healing only, as the RWD for CTL and *NF1*-mutant hiMGL cells was decreased by ~50% after 4h, whereas inhibitor-induced reduction in RWD was no longer visible after 24h. P2RX4 blockade led to a reduction in both initial and late ATP-induced wound healing, whereas P2RX7 inhibition did not affect ATP-induced motility. Notably, there were no differences in the impact of P2 receptor blockers on motility between CTL and *NF1*-mutant hiMGL cells, excluding the possibility that differences in P2 receptor activation account for the reduced motility observed in *NF1*-mutant hiMGL cells. This conclusion is further supported by our observation that *P2ry12* (**Fig. 2B**), *P2rx4* and *P2rx7* (**Fig. S7A**) mRNA expression levels are similar in CTL and *NF1*-mutant hiMGL cells.

To further investigate microglia motility, we chose to focus on Toll-like receptor 2 (*TLR2*) activation, which is known to increase random movement of murine microglia (Ifuku et al., 2016). *TLR2* RNA expression was similar between CTL and *NF1*-mutant hiMGL cells (**Fig. S8A**). hiMGL cells were incubated for 48h with a known TLR2 ligand, PAM2CSK4 (PAM2; 100 ng/ml), prior to the scratch wound. While CTL and *NF1*-mutant hiMGL cells exhibited similar increases in motility following PAM2 stimulation, *NF1*-mutant hiMGL cells had ~30% reduced baseline motility relative to their CTL counterparts (**Fig. S8B**). In contrast, a related toll-like receptor, TLR8, was transcriptionally expressed at similar levels in all hiMGL cells and microglia motility in response to the TLR8 activator (506) did not differ between CTL and *NF1*-mutant hiMGL cells (**Fig. S8C, D)**. These findings support a selective impairment in hiMGL cell function in the setting of *NF1* mutation.

Induced phagocytosis is impaired in NF1*-mutant hiMGL cells*

In addition to their intrinsic electrophysiologic properties, microglia interact with other cells in the brain through phagocytosis and motility. First, to examine the phagocytic activity of CTL and *NF1*-mutant hiMGL cells in response to P2RY6-dependent UDP stimulation (Koizumi et al., 2007), we measured *P2RY6* RNA expression in CTL and *NF1*-mutant hiMGL cells and found no differences between the two groups (**Fig. 7A**). Second, we quantified phagocytosis in at least three independent sets of CTL and *NF1*-mutant hiMGL cells following incubation for 45 minutes with yellow-green fluorescent Fluoresbrite carboxylate polystyrene beads (**Fig. 7B**). While M2 hiMGL cells showed a ~50% increase in baseline phagocytic index relative to CTL cells, UDP exclusively increased phagocytic activity in CTL hiMGL cells, but not in the *NF1*-mutant hiMGL cells.

To further study phagocytic activity in CTL and *NF1*-mutant hiMGL cells, we tested *TLR4* activation by LPS (1 µg/ml; **Fig. S9**), since TLR4 is a major mediator of induced phagocytosis in response to LPS (Lee and Lee 2002). In these experiments, LPS increased phagocytosis in CTL hiMGL cells, but

failed to increase the phagocytic activity of the three *NF1*-mutant hiMGL cell lines. Taken together, these data suggest that *NF1*-mutant hiMGL cells sense some extracellular signals (UDP, LPS), but do not activate the intracellular pathways necessary to increase phagocytic capacity. Additional studies will be required to define the signaling defects conferred by *NF1* mutation in hiMGL cells.

Discussion

In this study, we evaluated the impact of three different NF1 patient-derived germline *NF1* gene mutations on human iPSC-derived microglia function. Although we found no major changes in the microglial transcriptome, basal membrane currents, or cytokine secretion relative to their control counterparts, heterozygous *NF1* mutation (as seen in non-neoplastic cells from patients with NF1) caused alterations in hiMGL cell P2X-dependent purinergic signaling, phagocytic activity and motility *in vitro*. These findings are in contrast to what we observed in mouse *Nf1*-mutant microglia, which exhibited no defects in P2X purinergic membrane currents (Elmadany et al., 2020b). Instead, male mouse *Nf1*-mutant microglia had impaired P2Y purinergic membrane currents and cAMP generation, whereas their human *NF1*-mutant iMGL cell counterparts exhibited P2Y-mediated currents and cyclic AMP levels indistinguishable from CTL hiMGL cells. The observations reported herein highlight the differences in the effects of germline *NF1* mutations on mouse and human microglia function.

While the exact etiologies for these differences remain unelucidated, several possibilities exist. First, the prior experiments on *Nf1*+/- mouse microglia were performed on brain slices *in situ*, in which microglia can respond to local signals from other *Nf1*-mutant cell types (e.g., neurons). In this regard, microglia are very sensitive to environmental changes and can alter their expression profile within hours following removal from the brain (Gosselin et al., 2017). For instance, microglia markers, such as *P2RY12*, *CX3CR1* and *CD11B*, are downregulated during brain microglia isolation (Mizee et al., 2017). In addition, some transcripts expressed by microglia *in situ* using laser capture microdissection (LCM) are not found following FACS isolation (Solga et al., 2015b). Moreover, microglia maintained *in vitro* can express cytokine transcripts not expressed *in vivo* (Hurley et al., 1999), such that enzymatic dissociation can induce transcriptional bias not reflective of their *in vivo* state (Mattei et al., 2020).

Second, it is conceivable that the hiMGL cells are not fully mature as a result of *in vitro* differentiation and lack some of the functional properties seen in their adult (12-16 week old) mouse counterparts. Since these microglia were induced through the differentiation of HPCs using defined soluble factors, they did not derive from the yolk sac and mature in the context of a developing brain. In support of this notion, human iPSC-derived microglia adopt a more *in vivo*-like expression pattern following transplantation into the mouse brain (Xu et al., 2020).

Third, there could be species-specific differences between human and mouse microglia relevant to inflammatory responses, as well as factors involved in brain development (Galatro et al., 2017; Gerrits et al., 2020; Jurga et al., 2020; Smith and Dragunow, 2014). Other studies found greater heterogeneity in human microglia populations *ex vivo* compared to murine microglia. These differences likely relate to the shorter life span and more controlled living environment of laboratory animals (Abels et al., 2021; Galatro et al., 2017; Geirsdottir et al., 2019; Jurga et al., 2020). In a study analyzing glioma-associated microglia, differential expression of species-specific signaling molecules that mediate microglia-glioma interactions were noted. As such, the glioma growth-promoting cytokine, CCL18, is expressed by human microglia, but not by murine microglia. Additionally, murine microglia produce a significant amount of nitric oxide upon stimulation with LPS, while human microglia do not (Landry et al., 2012). Moreover, murine and human microglia have different, and sometimes even opposite, reactions to drug treatments. For example, valproic acid (VPA) induces cell death through caspase-3 activation in rodent, but not human, microglia. VPA has also been shown to increase phagocytic activity of rodent microglia, while inhibiting phagocytosis in human microglia (Gibbons et al., 2011; Smith et al., 2010). Lastly, murine microglia have higher proliferation capacities *in vitro* than human microglia do (Smith and Dragunow, 2014).

Taken together, the results described in this report reveal defects in human *NF1*-mutant microglia, as well as differences and similarities in function between human iMGL cells and mouse *Nf1*-mutant microglia. Future studies will be required to determine whether these similarities and differences reflect species-specific effects or the impact of the brain environment on microglia function *in vivo*.

Materials and Methods

hiPSC quality control. All hiPSC lines used in this project underwent extensive quality control before being used for microglial differentiation. Sterility for microorganisms was assessed first by antibiotic-free culture for a week. Cells were checked daily under the microscope and showed no signs of microbiological contamination. Next, cells were tested for Mycoplasma using the Promokine Mycoplasma Test Kit I/C. All cell lines used tested negative for contamination with mycoplasma, bacteria, yeast or fungi (data not shown). Viability appeared normal, and growth to confluence was typical of hiPSCs. Pluripotency of hiPSC was confirmed through immunocytochemistry for pluripotency markers (OCT3/4, NANOG, TRA-1-60 and SSEA-4, **Fig. S1**). hiPSCs were karyotyped using the ISCAN machine and the Illumina platform OMNI-Express-8v1.6 Chip (Maker coverage 958,497 spanning the whole human genome). The analysis was performed using the Karyostudio 1.3 software based on the information of GRCh36/hg18 dataset. All cell lines had an inconspicuous karyotype showing no larger areas of deletions or insertions (**Fig. S1)**. All alterations that were detected were well below the 5 megabase pair (Mbp) threshold detectable by regular G-banding. A 1.7

Mbp gain (chromosome 20) in the CTL hiPSC line was the largest gain found. A similar gain was found in all *NF1*-mutant lines (**Fig. S1**). Cell line identity (STR analysis) was performed using the GenePrint 10 System (Promega Corporation). The analysis confirmed that all hiPSC lines are derived from the same donor (data not shown).

hiPSC culture. hiPSCs were grown on Geltrex™-coated vessels (0,12-0,18 mg/ml, Life Technologies Corporation, Grand Island, NY, USA), incubated in StemMACS™ iPS-Brew XF (Miltenyi Biotec, Bergisch Gladbach, Germany), passaged weekly using StemPro® Accutase® (Life Technologies Corporation, Grand Island, NY, USA), and supplemented with 0.5 µM Thiazovivin (Stemcell Technologies™, Vancouver, BC, Canada) for the first 24 hours after passaging. hiPSCs were frozen in Bambanker (GC Lymphotec Inc., Tokyo, Japan) for long-term liquid nitrogen storage. hiPSCs used for microglial differentiation were kept in culture for a maximum of 3 weeks.

Microglial differentiation. hiMGL cells were generated from hiPSCs as previously described (McQuade et al., 2018) with minor modifications. On Day -1, about 60-100 hiPSC clusters were seeded onto a Geltrex™-coated 6-well plate (Falcon®, Corning, Glendale, AZ, USA) (**Fig. 1A**) with fresh StemMACS™ medium. On day 0 (induction), wells containing approximately 50 clusters at a diameter of 100-200µm each were used for hematopoietic differentiation. Hematopoietic progenitor cells (HPCs) were generated using the STEMdiff™ Hematopoietic Kit (StemCell Technologies, Vancouver, Canada). On day 0, media was changed to Medium A for the initial 3 days of the protocol. On day 3, Medium A was exchanged for Medium B and cells were cultured for an additional 9 days. The first HPCs arose on day 7. On day 12, HPCs that have been reported to be $CD43^+$ (McQuade et al., 2018) were harvested and replated ($1.2*10^5$/6-well) into DMEM/F12-based (no phenol red) (Life Technologies Corporation, Grand Island, NY, USA) serum-free microglia differentiation medium with B27 (2X) (Life Technologies Corporation, Grand Island, NY, USA), Insulin-Transferrin-Selenite (2X) (Life Technologies Corporation, Grand Island, NY, USA), N-2 (0.5X) (Life Technologies Corporation, Grand Island, NY, USA), GlutaMAX™ (1X) (Life Technologies Corporation, Grand Island, NY, USA), MEM NEAA (1X) (Life Technologies Corporation, Grand Island, NY, USA), Insulin (5 µg/ml) (PromoCell, Heidelberg, Germany) and α-Thioglycerol (400 µM) (Merck, Darmstadt, Germany). Microglia differentiation medium was supplemented with IL-34 (100 ng/ml) (Peprotech, Cranbury, NJ, USA), TGF-ß1 (50 ng/ml) (Peprotech, Cranbury, NJ, USA) and M-CSF (25 ng/ml) (Peprotech, Cranbury, NJ, USA). Medium with fresh supplements (IL-34, TGF-ß1, M-CSF) was added every other day. On day 12 and day 25 after replating the HPCs, excess media was carefully removed, leaving 3 ml/well behind. On day 25 and again on day 27 post replating, CD200 (100 ng/ml) (Novoprotein America Inc., Fremont, CA, USA) and Fractalkine (100 ng/ml) (Peprotech, Cranbury, NJ, USA) were additionally added to the media to support microglial maturation. hiMGL

cells were harvested between days 40 and 43 post induction (days 28 and 31 post replating, respectively).

Immunocytochemistry. hiMGL cells were seeded onto 12 mm glass coverslips in 24-well plates (Sarstedt, Nümbrecht, Germany). Cells were fixed, washed with PBS, and treated with blocking solution, 5% normal donkey serum (Merck, Darmstadt, Germany) and 0.1% Triton® X 100 (Roth, Karlsruhe, Germany), for 1 h. Cells were incubated with primary antibody overnight at 4 °C (**Table S1**). Subsequently, they were washed 3x with PBS incubated with an appropriate secondary antibody for 2h at room temperature. Nuclei were counterstained with 4′,6-diamidino-2-phenylindole (DAPI) solution (Merck, Darmstadt, Germany) for 20 min. Cells were washed 3x with PBS and coverslips attached onto glass slides using 1 drop of Aqua-Poly/Mount (Polysciences Europe GmbH, Hirschberg an der Bergstraße, Germany). Pictures were acquired using a Leica DMi8 Thunder Imager 3D microscope with a Leica DMC 2900 camera or a Leica DMi8 microscope with a Leica DFC450 C camera (Leica Microsystems, Wetzlar, Germany).

Quantitative RT-PCR. For gene expression analysis, cells were harvested and RNA was isolated with the ReliaPrep RNA Tissue Kit (Promega, Fitchburg, USA) according to manufacturer's instructions. RNA purity and concentration were measured using a NanoDrop 8000 spectrometer (Thermo Fisher Scientific, Schwerte, Germany) and RNA was reverse-transcribed into cDNA using PrimeScript RT Reagent Kit (Takara Bio Inc., Kusatsu, Japan). Duplicate quantitative polymerase chain reaction (qPCR) were performed with 7500 Fast Real-Time thermocycler (Applied Biosystems, Carlsbad, USA) using the SYBR Green Master Mix (Life Technologies Corporation, Grand Island, NY, USA). TATA box-binding protein (*TBP*) was used as the housekeeping gene (**Table S2**). Ct values were recorded for each sample for the target gene and the housekeeping gene and ΔCT values were calculated. Expression was shown relative to the expression of the housekeeping gene or CTL hiMGL cells.

Scratch Wound Assay. Cell motility was assessed using the IncuCyte® Cell Migration kit (Sartorius, Göttingen, Germany) and an Incucyte® Zoom Live Cell Analysis System (Sartorius, Göttingen, Germany). 100,000 hiMGL cells were seeded onto a 96-well ImageLock™ plate (Sartorius, Göttingen, Germany) and incubated for 4 h in serum-free microglia maturation media supplemented with IL-34, TGF-ß1, M-CSF, CD200, Fractalkine. Scratches were then made in all wells simultaneously using the IncuCyte® Cell Migration kit (Sartorius, Göttingen, Germany) and plates placed into IncuCyte Zoom® Live Cell Analysis System, where hourly images were taken for 48 hours at 4X magnification. Data were acquired using the scratch wound analysis tool from the IncuCyte Zoom® software (Sartorius, Göttingen, Germany) and presented as Relative Wound Density (RWD, %).

For each experiment, a new processing definition was set by adjusting segmentation bias and setting a minimal object area of 500 µm^2. Confluency was measured and expressed as the percentage of scratch wound surface covered by the migrating cells. Confluency was normalized to 0% confluency at t=0.

Electrophysiological recordings. An Axioskop FS2plus (Zeiss, Oberkochen, Germany), a conventional patch-clamp amplifier (EPC9, HEKA Elektronik, Lambrecht, Germany) and TIDA 5.23 software (HEKA Elektronik, Lambrecht, Germany) were used. Patch pipettes were pulled from borosilicate glass with resistances of 3 - 8 MOhm. The following intracellular solution was used (in mM): KCl, 130; $MgCl_2$, 2; $CaCl_2$, 0.5; Na-ATP, 2; EGTA, 5; HEPES, 10; and had an osmolarity of 310 - 320 mOsm/l adjusted to a pH of 7.3 with KOH. The extracellular solution contained (in mM): NaCl, 140; KCl, 5; $MgCl_2$, 1; $CaCl_2$, 2; HEPES, 10; D-glucose, 10; pH 7.4; 270 - 290 mOsm/L. Experiments with series resistances less than 100 MOhm were used for data analysis. All experiments were performed in the voltage-clamp configuration. To obtain current-voltage curves during continuous recordings, the membrane was clamped every for 5 s from a holding potential of either -70 mV (membrane properties**; Fig. S6**) or -20 mV (ATP responses; **Fig. 4** and **Fig. 5**) to a series of 50 ms de- and hyperpolarizing voltages ranging from -140 mV to 60 mV with 10 mV or 20 mV increment. Membrane currents were averaged for quantification between 30 and 45 ms after clamping the membrane to a given value from the resting potential. Membrane capacitance was quantified based on an exponential fit of the current decay in response to a -10 mV test pulse. The same pulse was used to quantify series resistance from the peak amplitude of the membrane capacitance currents. Comparisons of membrane currents between different groups were normalized to the membrane capacitance.

In vitro phagocytosis assay. The phagocytosis assays were performed as previously described in (Pannell et al., 2016) with some adaptations. hiMGL cells were seeded onto glass coverslips in a 24-well plate (2.5*10^5/well) and incubated in serum-free microglia maturation media supplemented with IL-34, TGF-ß1, M-CSF, CD200 and Fractalkine for 4h and were stimulated with 1 µg/ml Lipopolysaccharide (LPS, Merck, Darmstadt, Germany) or none. Yellow-green fluorescent Fluoresbrite® carboxylated microbeads (3.00 µm diameter, Polysciences Europe GmbH, Hirschberg an der Bergstraße, Germany) were pre-opsonized with fetal calf serum (FCS, Life Technologies Corporation, Grand Island, NY, USA) by shaking at 1000 rpm for 30 min at room temperature. After centrifugation for 2 min at 900 g, the supernatant was discarded and microbeads were washed and resuspended in HBSS (Life Technologies Corporation, Grand Island, NY, USA). hiMGL cells were incubated with the microbead suspension (approximately 4.8*10^6 microbeads/well) containing either no stimulant (basal), UDP (100 µM) or LPS (1 µg/ml) for 45 min. Cells were then washed with PBS (Life Technologies Corporation, Grand Island, NY, USA). Coverslips were fixed with 4%

paraformaldehyde, washed and blocked in TBS containing 5% donkey serum and 0.1% Triton® X 100 for 1 h. Cells were next stained with anti-IBA1 antibodies (**Table S1**) in TBS containing 5% donkey serum overnight. After washing, cells were incubated with a secondary Alexa Fluor 647 antibody (**Table S1**) and DAPI before mounting with Aqua-Poly/Mount. Three z-stack images per coverslip were acquired using a Leica TCS SPE confocal laser microscope (Leica microsystems, Wetzlar, Germany). Images were 3D-rendered using Imaris software (Imaris 9, Oxford instruments, Abingdon, UK). IBA1 surfaces and spots for DAPI and microbeads were created. Representing the hiMGL cell number per image DAPI within IBA1 surfaces were assessed using the split into object function. Representing the phagocytosed beads, the number of beads within IBA1 surfaces were counted. Using in-house developed Python software, cells were grouped to 0, 0-1, 1-2, 2-3, >3 or more beads per cell. The percentage of cells in each group was multiplied by the corresponding grade of phagocytosis: 0: 1, 0-1: 2, 1-2: 3, 2-3: 4, >3: 5. The sum of the products in each group was then defined as the phagocytosis index (PI).

cAMP ELISA. cAMP levels in hiMGL cells were determined using the cyclic AMP ELISA Kit (Cayman chemical, Ann Arbor, MI, USA) according to the manufacturer's instructions. Briefly, hiMGL cells were resuspended in 100 µl HCl (0.1 M) and centrifuged for 10 min at 1000 g. Supernatants were neutralized with ELISA buffer at a ratio of 1:2. Next, sample acetylation was performed by adding 60 µl KOH (4 M) and 15 µl acetic anhydride, vortexing for 15 s, followed by the addition of 15 µl KOH (4 M). Samples and standards were pipetted into the ELISA plates and incubated for 18 h at 4°C before the plate was developed with Ellmann's reagent. Fluorescence was measured at 420 nm using a Tecan infinite M200 plate reader (Tecan Group Ltd., Männedorf, Switzerland)

Multiplex ELISA. The cell supernatant (25 µl) was analyzed using the MagPix System (Luminex/Merck). The HCYTA-60K MILLIPLEX® MAP Human Cytokine/Chemokine/Growth Factor Panel A – Immunology Multiplex Assay was used according to the manufacturer's recommendations. The following analytes were included in the analysis: GM-CSF, GRO, IL-1β, IL-6, IL-10, IP-10, MCP-1, MCP-3, MIP-1α, MIP-1β, RANTES and TNFα. Xponent (Luminex) and Milliplex Analyst (Merck) software was used for data acquisition. Background (pure medium) was subtracted from the mean fluorescent intensities (MFI). Concentration (pg/ml) was determined using an 8 point calibration curve including matrix (cell culture media). The standards were measured twice. Samples were measured only once. For determining the instrumental variance pooled samples were used as quality control.

RNA sequencing and analysis. RNA was extracted from at four independently generated hiMGL cell cultures for each genotype (CTL, M1, M3) and subjected to sequencing on an Illumina HiSeq

platform. RNA sequencing analysis was generated using Partek Flow software, v10.0. RNA sequencing reads were aligned to the hg38 Ensembl release 105 assembly with STAR v2.7.8a. Gene counts and isoform expression were derived from Ensembl output. Sequencing performance was assessed for the total number of aligned reads, total number of uniquely aligned reads, and features detected. Normalization size factors were calculated for all gene counts by median ratio. Differential genetic analysis was then performed using DESeq2 to analyze for differences between conditions. Results were filtered for only those genes with false discovery rates ≤ .05 and fold changes more extreme than ± 5. Additional analyses were performed with 2- and 3-fold cutoff criteria. These data have been deposited in GEO (accession number GSE233373).

Statistics. Data are expressed as mean ± SEM. A combination of one-way ANOVA tests followed by a Dunnett's post hoc test or Tukey's multiple comparisons test was employed to compare data between more than 2 experimental groups. Student's t-test was used to compare data between 2 experimental conditions. IGOR Pro 6.34 or GraphPad Prism 9 (GraphPad Software, San Diego, CA, USA) were used for statistical analysis. Information about the statistical tests, number of experiments is specified in the figure legends. Significance levels are given as ***/### $p < 0.001$, **/## $p < 0.01$, */# $p < 0.05$, n.s. $p > 0.05$.

Acknowledgements

We thank Regina Piske, Maren Wendt, Nadine Scharek and Orhun Utku Aydin for technical assistance. We further thank the microscopy core facility (Advanced Light Microscopy, ALM) of the MDC Berlin and the Technology Platform Pluripotent Stem Cells of the MDC Berlin for technical assistance. We acknowledge Jennifer Kirwan from the Berlin Institute of Health Metabolomics Platform for providing the MagPix Instrument.

Competing Interest

No competing interests declared.

Funding

The work was supported by the NeuroCure Cluster of Excellence grant to H.K., a National Institute of Health grant (R35NS097211 to D.H.G) and a Berlin Institute of Health/Einstein fellowship grant to D.H.G. and H.K. D.H.G. is an Alexander von Humboldt Fellow.

References

Abels, E.R., Nieland, L., Hickman, S., Broekman, M.L.D., El Khoury, J., Maas, S.L.N., 2021. Comparative Analysis Identifies Similarities between the Human and Murine Microglial Sensomes. Int. J. Mol. Sci. 22, 1495. https://doi.org/10.3390/ijms22031495

Anastasaki, C., Wegscheid, M.L., Hartigan, K., Papke, J.B., Kopp, N.D., Chen, J., Cobb, O., Dougherty, J.D., Gutmann, D.H., 2020. Human iPSC-Derived Neurons and Cerebral Organoids Establish Differential Effects of Germline NF1 Gene Mutations. Stem Cell Rep. 14, 541–550. https://doi.org/10.1016/j.stemcr.2020.03.007

Boucsein, C., Kettenmann, H., Nolte, C., 2000. Electrophysiological properties of microglial cells in normal and pathologic rat brain slices. Eur. J. Neurosci. 12, 2049–2058. https://doi.org/10.1046/j.1460-9568.2000.00100.x

Butovsky, O., Jedrychowski, M.P., Moore, C.S., Cialic, R., Lanser, A.J., Gabriely, G., Koeglsperger, T., Dake, B., Wu, P.M., Doykan, C.E., Fanek, Z., Liu, L., Chen, Z., Rothstein, J.D., Ransohoff, R.M., Gygi, S.P., Antel, J.P., Weiner, H.L., 2014. Identification of a unique TGF-β-dependent molecular and functional signature in microglia. Nat. Neurosci. 17, 131–143. https://doi.org/10.1038/nn.3599

Costa, A., Haage, V., Yang, S., Wegner, S., Ersoy, B., Ugursu, B., Rex, A., Kronenberg, G., Gertz, K., Endres, M., Wolf, S.A., Kettenmann, H., 2021. Deletion of muscarinic acetylcholine receptor 3 in microglia impacts brain ischemic injury. Brain. Behav. Immun. 91, 89–104. https://doi.org/10.1016/j.bbi.2020.09.008

Daginakatte, G.C., Gianino, S.M., Zhao, N.W., Parsadanian, A.S., Gutmann, D.H., 2008. Increased c-Jun-NH2-kinase signaling in neurofibromatosis-1 heterozygous microglia drives microglia activation and promotes optic glioma proliferation. Cancer Res. 68, 10358–10366. https://doi.org/10.1158/0008-5472.CAN-08-2506

de Andrade Costa, A., Chatterjee, J., Cobb, O., Cordell, E., Chao, A., Schaeffer, S., Goldstein, A., Dahiya, S., Gutmann, D.H., 2022. Immune deconvolution and temporal mapping identifies stromal targets and developmental intervals for abrogating murine low-grade optic glioma formation. Neuro-Oncol. Adv. 4, vdab194. https://doi.org/10.1093/noajnl/vdab194

Derecki, N.C., Cronk, J.C., Lu, Z., Xu, E., Abbott, S.B.G., Guyenet, P.G., Kipnis, J., 2012. Wild-type microglia arrest pathology in a mouse model of Rett syndrome. Nature 484, 105–109. https://doi.org/10.1038/nature10907

Elmadany, N., de Almeida Sassi, F., Wendt, S., Logiacco, F., Visser, J., Haage, V., Hernandez, D.P., Mertins, P., Hambardzumyan, D., Wolf, S., Kettenmann, H., Semtner, M., 2020a. The VGF-derived Peptide TLQP21 Impairs Purinergic Control of Chemotaxis and Phagocytosis in Mouse Microglia. J. Neurosci. Off. J. Soc. Neurosci. 40, 3320–3331. https://doi.org/10.1523/JNEUROSCI.1458-19.2020

Elmadany, N., Logiacco, F., Buonfiglioli, A., Haage, V.C., Wright-Jin, E.C., Schattenberg, A., Papawassiliou, R.M., Kettenmann, H., Semtner, M., Gutmann, D.H., 2020b. Neurofibromatosis 1 - Mutant microglia exhibit sexually-dimorphic cyclic AMP-dependent purinergic defects. Neurobiol. Dis. 144, 105030. https://doi.org/10.1016/j.nbd.2020.105030

Galatro, T.F., Holtman, I.R., Lerario, A.M., Vainchtein, I.D., Brouwer, N., Sola, P.R., Veras, M.M., Pereira, T.F., Leite, R.E.P., Möller, T., Wes, P.D., Sogayar, M.C., Laman, J.D., den Dunnen, W., Pasqualucci, C.A., Oba-Shinjo, S.M., Boddeke, E.W.G.M., Marie, S.K.N., Eggen, B.J.L., 2017. Transcriptomic analysis of purified human cortical microglia reveals age-associated changes. Nat. Neurosci. 20, 1162–1171. https://doi.org/10.1038/nn.4597

Geirsdottir, L., David, E., Keren-Shaul, H., Weiner, A., Bohlen, S.C., Neuber, J., Balic, A., Giladi, A., Sheban, F., Dutertre, C.-A., Pfeifle, C., Peri, F., Raffo-Romero, A., Vizioli, J., Matiasek, K., Scheiwe, C., Meckel, S., Mätz-Rensing, K., van der Meer, F., Thormodsson, F.R., Stadelmann, C., Zilkha, N., Kimchi, T., Ginhoux, F., Ulitsky, I., Erny, D., Amit, I., Prinz, M., 2020. Cross-Species Single-Cell Analysis Reveals Divergence of the Primate Microglia Program. Cell 181, 746. https://doi.org/10.1016/j.cell.2020.04.002

Geirsdottir, L., David, E., Keren-Shaul, H., Weiner, A., Bohlen, S.C., Neuber, J., Balic, A., Giladi, A., Sheban, F., Dutertre, C.-A., Pfeifle, C., Peri, F., Raffo-Romero, A., Vizioli, J., Matiasek, K., Scheiwe, C., Meckel, S., Mätz-Rensing, K., van der Meer, F., Thormodsson, F.R., Stadelmann, C., Zilkha, N., Kimchi, T., Ginhoux, F., Ulitsky, I., Erny, D., Amit, I., Prinz, M., 2019. Cross-Species Single-Cell Analysis Reveals Divergence of the Primate Microglia Program. Cell 179, 1609-1622.e16. https://doi.org/10.1016/j.cell.2019.11.010

Gerrits, E., Heng, Y., Boddeke, E.W.G.M., Eggen, B.J.L., 2020. Transcriptional profiling of microglia; current state of the art and future perspectives. Glia 68, 740–755. https://doi.org/10.1002/glia.23767

Gibbons, H.M., Smith, A.M., Teoh, H.H., Bergin, P.M., Mee, E.W., Faull, R.L.M., Dragunow, M., 2011. Valproic acid induces microglial dysfunction, not apoptosis, in human glial cultures. Neurobiol. Dis. 41, 96–103. https://doi.org/10.1016/j.nbd.2010.08.024

Ginhoux, F., Greter, M., Leboeuf, M., Nandi, S., See, P., Gokhan, S., Mehler, M.F., Conway, S.J., Ng, L.G., Stanley, E.R., Samokhvalov, I.M., Merad, M., 2010. Fate mapping analysis reveals that adult microglia derive from primitive macrophages. Science 330, 841–845. https://doi.org/10.1126/science.1194637

Gosselin, D., Skola, D., Coufal, N.G., Holtman, I.R., Schlachetzki, J.C.M., Sajti, E., Jaeger, B.N., O'Connor, C., Fitzpatrick, C., Pasillas, M.P., Pena, M., Adair, A., Gonda, D.G., Levy, M.L., Ransohoff, R.M., Gage, F.H., Glass, C.K., 2017. An environment-dependent transcriptional network specifies human microglia identity. Science 356, eaal3222. https://doi.org/10.1126/science.aal3222

Guo, X., Pan, Y., Gutmann, D.H., 2019. Genetic and genomic alterations differentially dictate low-grade glioma growth through cancer stem cell-specific chemokine recruitment of T cells and microglia. Neuro-Oncol. 21, 1250–1262. https://doi.org/10.1093/neuonc/noz080

Hambardzumyan, D., Gutmann, D.H., Kettenmann, H., 2016. The role of microglia and macrophages in glioma maintenance and progression. Nat. Neurosci. 19, 20–27. https://doi.org/10.1038/nn.4185

Hammond, T.R., Dufort, C., Dissing-Olesen, L., Giera, S., Young, A., Wysoker, A., Walker, A.J., Gergits, F., Segel, M., Nemesh, J., Marsh, S.E., Saunders, A., Macosko, E., Ginhoux, F., Chen, J., Franklin, R.J.M., Piao, X., McCarroll, S.A., Stevens, B., 2019. Single-Cell RNA Sequencing of Microglia throughout the Mouse Lifespan and in the Injured Brain Reveals Complex Cell-State Changes. Immunity 50, 253-271.e6. https://doi.org/10.1016/j.immuni.2018.11.004

Hoeffel, G., Ginhoux, F., 2015. Ontogeny of Tissue-Resident Macrophages. Front. Immunol. 6, 486. https://doi.org/10.3389/fimmu.2015.00486

Hong, S., Beja-Glasser, V.F., Nfonoyim, B.M., Frouin, A., Li, S., Ramakrishnan, S., Merry, K.M., Shi, Q., Rosenthal, A., Barres, B.A., Lemere, C.A., Selkoe, D.J., Stevens, B., 2016. Complement and microglia mediate early synapse loss in Alzheimer mouse models. Science 352, 712–716. https://doi.org/10.1126/science.aad8373

Hurley, S.D., Walter, S.A., Semple-Rowland, S.L., Streit, W.J., 1999. Cytokine transcripts expressed by microglia in vitro are not expressed by ameboid microglia of the developing rat central nervous system. Glia 25, 304–309. https://doi.org/10.1002/(sici)1098-1136(19990201)25:3<304::aid-glia10>3.0.co;2-w

Jairaman, A., McQuade, A., Granzotto, A., Kang, Y.J., Chadarevian, J.P., Gandhi, S., Parker, I., Smith, I., Cho, H., Sensi, S.L., Othy, S., Blurton-Jones, M., Cahalan, M.D., 2022. TREM2 regulates purinergic receptor-mediated calcium signaling and motility in human iPSC-derived microglia. eLife 11, e73021. https://doi.org/10.7554/eLife.73021

Jurga, A.M., Paleczna, M., Kuter, K.Z., 2020. Overview of General and Discriminating Markers of Differential Microglia Phenotypes. Front. Cell. Neurosci. 14, 198. https://doi.org/10.3389/fncel.2020.00198

Kana, V., Desland, F.A., Casanova-Acebes, M., Ayata, P., Badimon, A., Nabel, E., Yamamuro, K., Sneeboer, M., Tan, I.-L., Flanigan, M.E., Rose, S.A., Chang, C., Leader, A., Le Bourhis, H., Sweet, E.S., Tung, N., Wroblewska, A., Lavin, Y., See, P., Baccarini, A., Ginhoux, F., Chitu, V., Stanley, E.R., Russo, S.J., Yue, Z., Brown, B.D., Joyner, A.L., De Witte, L.D., Morishita, H., Schaefer, A., Merad, M., 2019. CSF-1 controls cerebellar microglia and is required for motor function and social interaction. J. Exp. Med. 216, 2265–2281. https://doi.org/10.1084/jem.20182037

Kettenmann, H., Hanisch, U.-K., Noda, M., Verkhratsky, A., 2011. Physiology of microglia. Physiol. Rev. 91, 461–553. https://doi.org/10.1152/physrev.00011.2010

Koizumi, S., Shigemoto-Mogami, Y., Nasu-Tada, K., Shinozaki, Y., Ohsawa, K., Tsuda, M., Joshi, B.V., Jacobson, K.A., Kohsaka, S., Inoue, K., 2007. UDP acting at P2Y6 receptors is a mediator of microglial phagocytosis. Nature 446, 1091–1095. https://doi.org/10.1038/nature05704

Landry, R.P., Jacobs, V.L., Romero-Sandoval, E.A., DeLeo, J.A., 2012. Propentofylline, a CNS glial modulator does not decrease pain in post-herpetic neuralgia patients: in vitro evidence for differential responses in human and rodent microglia and macrophages. Exp. Neurol. 234, 340–350. https://doi.org/10.1016/j.expneurol.2011.11.006

Leyns, C.E.G., Gratuze, M., Narasimhan, S., Jain, N., Koscal, L.J., Jiang, H., Manis, M., Colonna, M., Lee, V.M.Y., Ulrich, J.D., Holtzman, D.M., 2019. TREM2 function impedes tau seeding in neuritic plaques. Nat. Neurosci. 22, 1217–1222. https://doi.org/10.1038/s41593-019-0433-0

Logiacco, F., Grzegorzek, L.C., Cordell, E.C., Popp, O., Mertins, P., Gutmann, D.H., Kettenmann, H., Semtner, M., 2023. Neurofibromatosis type 1-dependent alterations in mouse microglia function are not cell-intrinsic. Acta Neuropathol. Commun. 11, 36. https://doi.org/10.1186/s40478-023-01525-w

Marsh, S.E., Walker, A.J., Kamath, T., Dissing-Olesen, L., Hammond, T.R., de Soysa, T.Y., Young, A.M.H., Murphy, S., Abdulraouf, A., Nadaf, N., Dufort, C., Walker, A.C., Lucca, L.E., Kozareva, V., Vanderburg, C., Hong, S., Bulstrode, H., Hutchinson, P.J., Gaffney, D.J., Hafler, D.A., Franklin, R.J.M., Macosko, E.Z., Stevens, B., 2022. Dissection of artifactual and confounding glial signatures by single-cell sequencing of mouse and human brain. Nat. Neurosci. 25, 306–316. https://doi.org/10.1038/s41593-022-01022-8

Mattei, D., Ivanov, A., van Oostrum, M., Pantelyushin, S., Richetto, J., Mueller, F., Beffinger, M., Schellhammer, L., Vom Berg, J., Wollscheid, B., Beule, D., Paolicelli, R.C., Meyer, U., 2020. Enzymatic Dissociation Induces Transcriptional and Proteotype Bias in Brain Cell Populations. Int. J. Mol. Sci. 21, E7944. https://doi.org/10.3390/ijms21217944

McQuade, A., Blurton-Jones, M., 2022. Human Induced Pluripotent Stem Cell-Derived Microglia (hiPSC-Microglia). Methods Mol. Biol. Clifton NJ 2454, 473–482. https://doi.org/10.1007/7651_2021_429

McQuade, A., Coburn, M., Tu, C.H., Hasselmann, J., Davtyan, H., Blurton-Jones, M., 2018. Development and validation of a simplified method to generate human microglia from pluripotent stem cells. Mol. Neurodegener. 13, 67. https://doi.org/10.1186/s13024-018-0297-x

Mizee, M.R., Miedema, S.S.M., van der Poel, M., Adelia, null, Schuurman, K.G., van Strien, M.E., Melief, J., Smolders, J., Hendrickx, D.A., Heutinck, K.M., Hamann, J., Huitinga, I., 2017. Isolation of primary microglia from the human post-mortem brain: effects of ante- and post-mortem variables. Acta Neuropathol. Commun. 5, 16. https://doi.org/10.1186/s40478-017-0418-8

Ousingsawat, J., Wanitchakool, P., Kmit, A., Romao, A.M., Jantarajit, W., Schreiber, R., Kunzelmann, K., 2015. Anoctamin 6 mediates effects essential for innate immunity downstream of P2X7 receptors in macrophages. Nat. Commun. 6, 6245. https://doi.org/10.1038/ncomms7245

Pan, Y., Xiong, M., Chen, R., Ma, Y., Corman, C., Maricos, M., Kindler, U., Semtner, M., Chen, Y.-H., Dahiya, S., Gutmann, D.H., 2018. Athymic mice reveal a requirement for T-cell-microglia interactions in establishing a microenvironment supportive of Nf1 low-grade glioma growth. Genes Dev. 32, 491–496. https://doi.org/10.1101/gad.310797.117

Pannell, M., Meier, M.A., Szulzewsky, F., Matyash, V., Endres, M., Kronenberg, G., Prinz, V., Waiczies, S., Wolf, S.A., Kettenmann, H., 2016. The subpopulation of microglia expressing functional muscarinic acetylcholine receptors expands in stroke and Alzheimer's disease. Brain Struct. Funct. 221, 1157–1172. https://doi.org/10.1007/s00429-014-0962-y

Pasqualini, C., Kozaki, T., Bruschi, M., Nguyen, T.H.H., Minard-Colin, V., Castel, D., Grill, J., Ginhoux, F., 2020. Modeling the Interaction between the Microenvironment and Tumor Cells in Brain Tumors. Neuron 108, 1025–1044. https://doi.org/10.1016/j.neuron.2020.09.018

Sierra, A., Paolicelli, R.C., Kettenmann, H., 2019. Cien Años de Microglía: Milestones in a Century of Microglial Research. Trends Neurosci. 42, 778–792. https://doi.org/10.1016/j.tins.2019.09.004

Smith, A.M., Dragunow, M., 2014. The human side of microglia. Trends Neurosci. 37, 125–135. https://doi.org/10.1016/j.tins.2013.12.001

Smith, A.M., Gibbons, H.M., Dragunow, M., 2010. Valproic acid enhances microglial phagocytosis of amyloid-beta(1-42). Neuroscience 169, 505–515. https://doi.org/10.1016/j.neuroscience.2010.04.041

Solga, A.C., Pong, W.W., Kim, K.-Y., Cimino, P.J., Toonen, J.A., Walker, J., Wylie, T., Magrini, V., Griffith, M., Griffith, O.L., Ly, A., Ellisman, M.H., Mardis, E.R., Gutmann, D.H., 2015a. RNA Sequencing of Tumor-Associated Microglia Reveals Ccl5 as a Stromal Chemokine Critical for Neurofibromatosis-1 Glioma Growth. Neoplasia N. Y. N 17, 776–788. https://doi.org/10.1016/j.neo.2015.10.002

Solga, A.C., Pong, W.W., Walker, J., Wylie, T., Magrini, V., Apicelli, A.J., Griffith, M., Griffith, O.L., Kohsaka, S., Wu, G.F., Brody, D.L., Mardis, E.R., Gutmann, D.H., 2015b. RNA-sequencing reveals oligodendrocyte and neuronal transcripts in microglia relevant to central nervous system disease. Glia 63, 531–548. https://doi.org/10.1002/glia.22754

Takata, K., Kozaki, T., Lee, C.Z.W., Thion, M.S., Otsuka, M., Lim, S., Utami, K.H., Fidan, K., Park, D.S., Malleret, B., Chakarov, S., See, P., Low, D., Low, G., Garcia-Miralles, M., Zeng, R., Zhang, J., Goh, C.C., Gul, A., Hubert, S., Lee, B., Chen, J., Low, I., Shadan, N.B., Lum, J., Wei, T.S., Mok, E., Kawanishi, S., Kitamura, Y., Larbi, A., Poidinger, M., Renia, L., Ng, L.G., Wolf, Y., Jung, S., Önder, T., Newell, E., Huber, T., Ashihara, E., Garel, S., Pouladi, M.A., Ginhoux, F., 2017. Induced-Pluripotent-Stem-Cell-Derived Primitive Macrophages Provide a Platform for Modeling Tissue-Resident Macrophage Differentiation and Function. Immunity 47, 183-198.e6. https://doi.org/10.1016/j.immuni.2017.06.017

Toonen, J.A., Anastasaki, C., Smithson, L.J., Gianino, S.M., Li, K., Kesterson, R.A., Gutmann, D.H., 2016. NF1 germline mutation differentially dictates optic glioma formation and growth in neurofibromatosis-1. Hum. Mol. Genet. 25, 1703–1713. https://doi.org/10.1093/hmg/ddw039

Toonen, J.A., Solga, A.C., Ma, Y., Gutmann, D.H., 2017. Estrogen activation of microglia underlies the sexually dimorphic differences in Nf1 optic glioma–induced retinal pathology. J. Exp. Med. 214, 17–25. https://doi.org/10.1084/jem.20160447

Wolf, S.A., Boddeke, H.W.G.M., Kettenmann, H., 2017. Microglia in Physiology and Disease. Annu. Rev. Physiol. 79, 619–643. https://doi.org/10.1146/annurev-physiol-022516-034406

Xu, R., Li, X., Boreland, A.J., Posyton, A., Kwan, K., Hart, R.P., Jiang, P., 2020. Human iPSC-derived mature microglia retain their identity and functionally integrate in the chimeric mouse brain. Nat. Commun. 11, 1577. https://doi.org/10.1038/s41467-020-15411-9

Figures

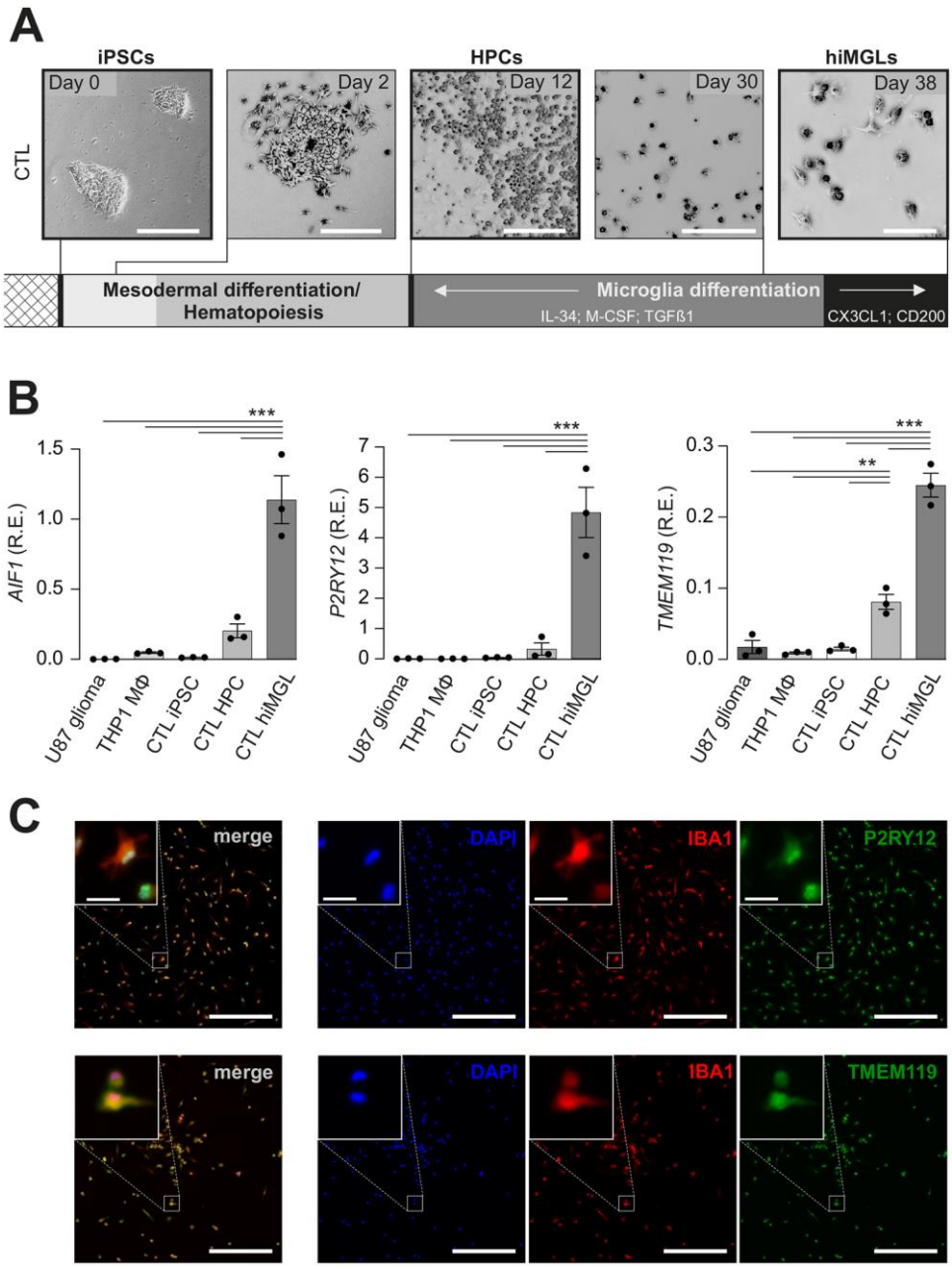

Fig. 1. hiMGL cell differentiation from CTL hiPSCs

A Representative bright field images of human induced microglia-like cells (hiMGL cells) differentiated from male BJFF.6 control (CTL) hiPSCs. Day 0: hiPSC cluster under regular hiPSC growth conditions. Mesodermal and hematopoietic differentiation was induced by StemCell Technologies STEMdiff™ Hematopoietic Kit. Day 2: Mesodermal differentiation. Day 12: Hematopoietic progenitor cells (HPC). Day 30: Microglial differentiation using serum-free basal media supplemented with IL-34 (100 ng/ml), M-CSF (25 ng/ml) and TGFß1 (50 ng/ml). Day 38: CX3CL1 (100 ng/ml) and CD200 (100 ng/ml) were additionally supplemented for hiMGL cell

maturation for the final three days *in vitro*. Scale bars in the images from day 0 to day 30 was 200 µm, while the scale bar for day 38 was 50 µm.

B Relative mRNA expression levels of microglial markers *AIF1*, *P2RY12 and TMEM119* were assessed in BJFF.6-derived control (CTL) hiPSCs, HPCs and hiMGL cells, as well as in THP-1-derived human macrophages (Mϕ) and U87 human glioma cells by quantitative RT-qPCR. Relative expression (R.E.) is shown relative to the TATA box binding protein (*TBP*) housekeeping gene (n=3). Results are represented as the mean ± SEM. Data were analyzed by one-way ANOVA followed by Tukey's multiple comparisons test. **P< 0.01, ***P<0.001.

C Immunohistochemical staining of BJFF.6-derived hiMGL cells with DAPI, as well as with IBA1 and the TMEM119 and P2RY12 microglia-specific antibodies. Merged images show the combined signal for DAPI, IBA1 and P2RY12 or TMEM119, respectively. Scale bars overview image: 200 µm. Scale bars inlay, 20 µm.

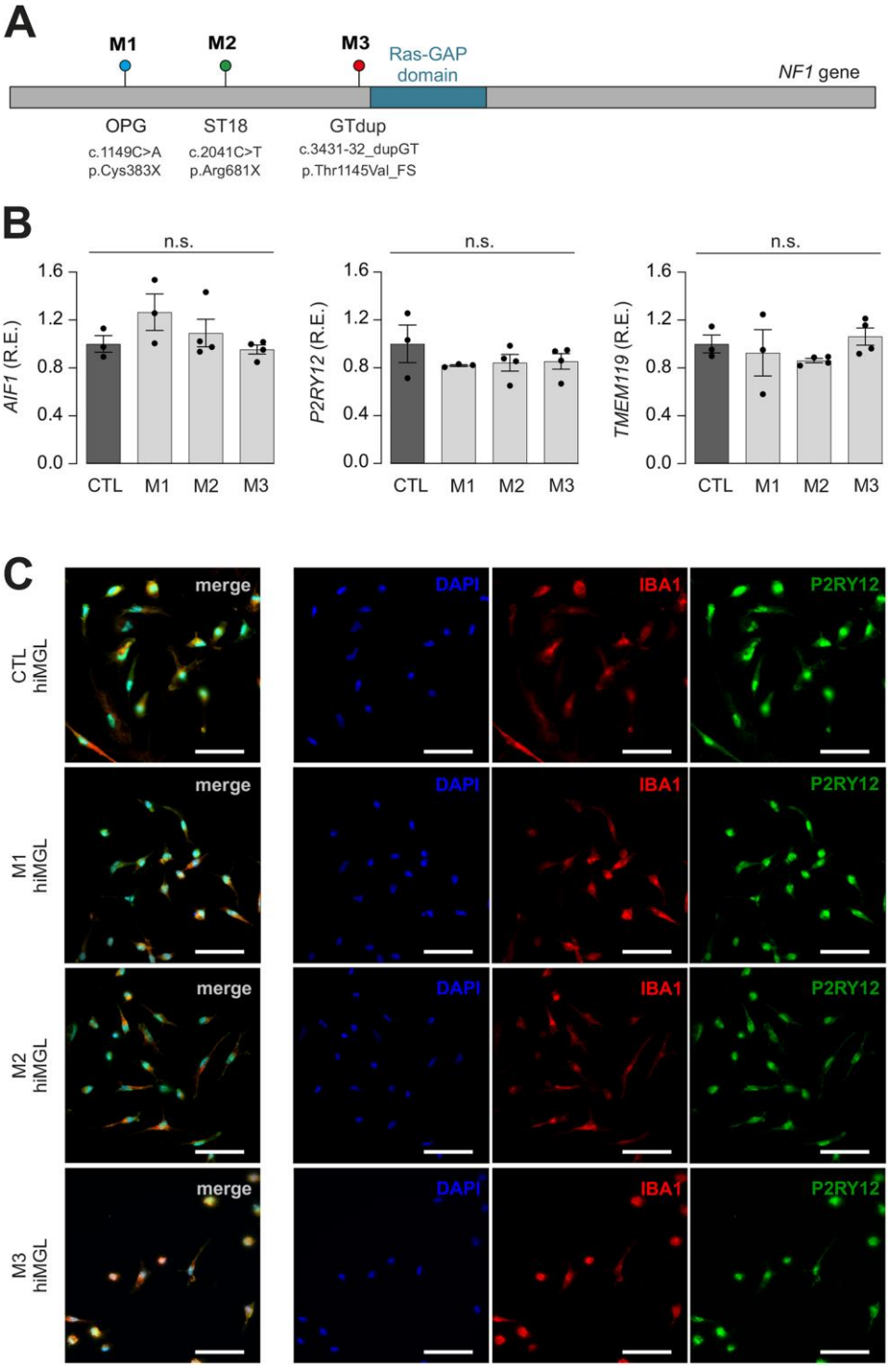

Fig. 2. *NF1*-mutant hiPSCs differentiate into human induced microglia-like (hiMGL) cells

A Lollipop plot depicting the location of mutations engineered into the *NF1* gene locus by CRISPR-Cas9 editing of CTL hiPSCs, generating three different *NF1*-mutant hiPSC lines. Mutant 1 (M1): OPG c.1149C>A p.Cys383X, M2: ST18 c.2041C>T p.Arg681X, M3: dup_GT c.3431-32_dupGT p.Thr1145Val_FS.

B Relative mRNA expression levels of *AIF1, P2RY12 and TMEM119* microglial markers were assessed in CTL and *NF1*-mutant hiMGL cells (M1-M3) by quantitative RT-PCR. Relative expression

(R.E.) is shown relative to CTL hiMGL cells. TATA box binding protein (*TBP*) was used as a housekeeping gene for normalization (n=3). Results are represented as the mean ± SEM. Data were analyzed using a one-way ANOVA followed by a Tukey's multiple comparisons test. No significant differences were found between CTL and M1-M3 hiMGL cells.

C Immunohistochemical staining of CTL and *NF1*-mutant (M1-M3) hiMGL cells for DAPI, IBA1 and P2RY12 expression. Merged images show the combined signal for DAPI, IBA1 and P2RY12. Scale bars, 50μm.

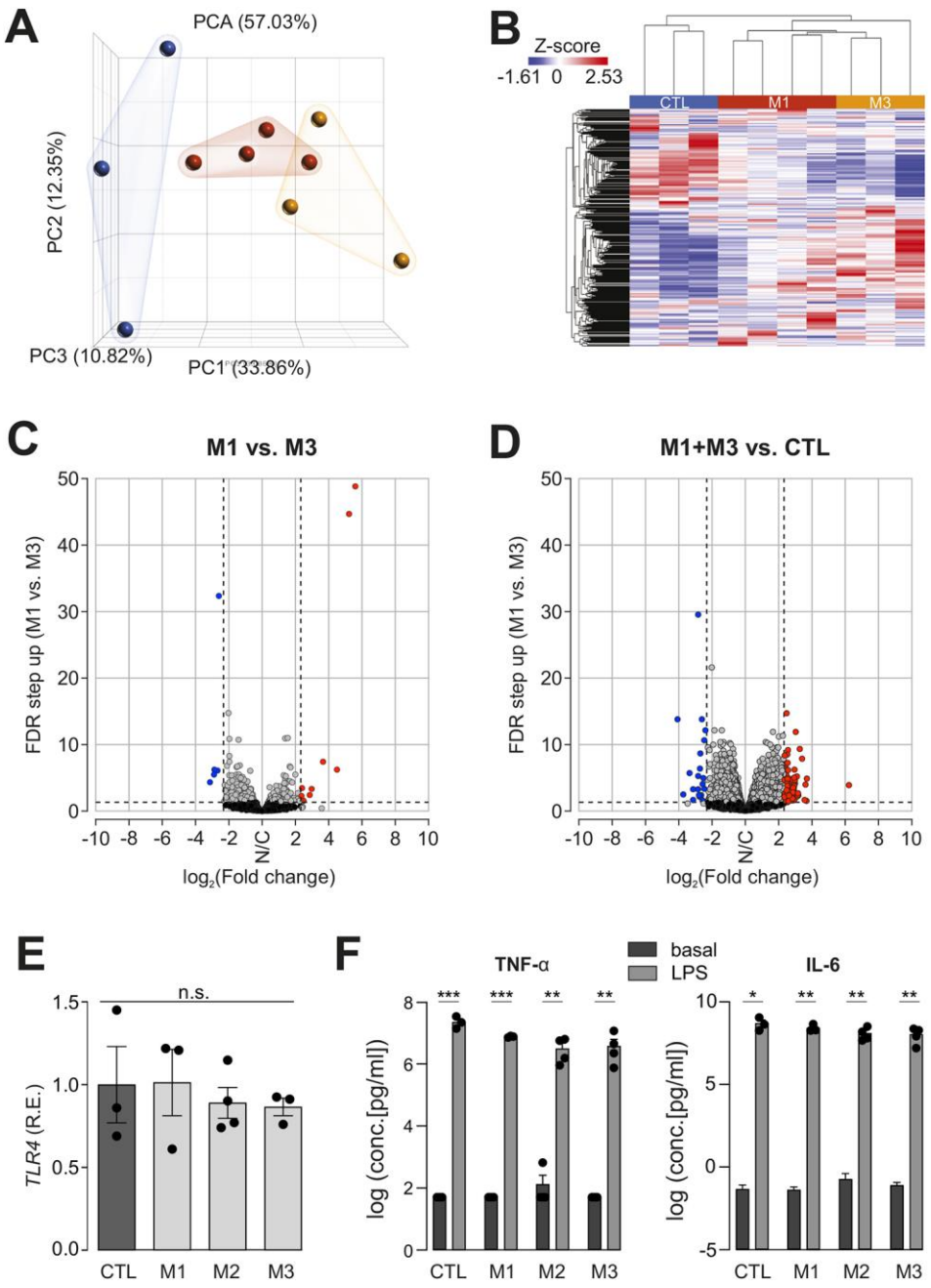

Fig. 3. RNAseq reveals few differences between *NF1*-mutant and CTL hiMGL cells, while the induced secretome remains unchanged

A PCA plot generated from RNA sequencing data (CTL, blue; M1, red; M3, yellow).

B Heatmap showing unsupervised hierarchical clustering generated from RNA sequencing data for CTL, M1 and M3 hiMGL cells.

C Volcano plot demonstrating genes differentially expressed between M1 versus M3 [FDR < .05; fold change (-5, 5)]. Grey dots (no change), blue dots (decreased expression), red dots (increased expression).

D Volcano plot demonstrating genes differentially expressed between M1 and M3 versus CTL [FDR < .05; fold change (-5, 5)]. Grey dots (no change), blue dots (decreased expression), red dots (increased expression).

E Relative mRNA expression of Toll-like receptor 4 (*TLR4*) in CTL and *NF1*-mutant (M1-M3) hiMGL cells by quantitative RT-PCR. Relative expression (R.E.) is shown relative to CTL hiMGL cells. TATA box binding protein (*TBP*) was used as a housekeeping gene for normalization (n=3). Data were normalized to *TLR4* expression of CTL hiMGL cells. Results are represented as the mean ± SD. Data were analyzed by one-way ANOVA.

F Multiplex immunoassay was used to detect TNF-α (left) and IL-6 (right) in supernatants from CTL and *NF1*-mutant (M1-M3) hiMGL cells in response to 1 μg/ml LPS stimulation for 24h (n = 3-4). Data between basal and LPS conditions were analyzed using unpaired t-tests. *P<0.05; **P<0.01, ***P<0.001. Results are represented as the mean ± SD. Cytokine release under basal or LPS conditions was not significantly different between CTL and M1, M2 and M3 hiMGL cells (one-way ANOVA; not shown). The data showing the release of additional cytokines is included in **Fig. S4**.

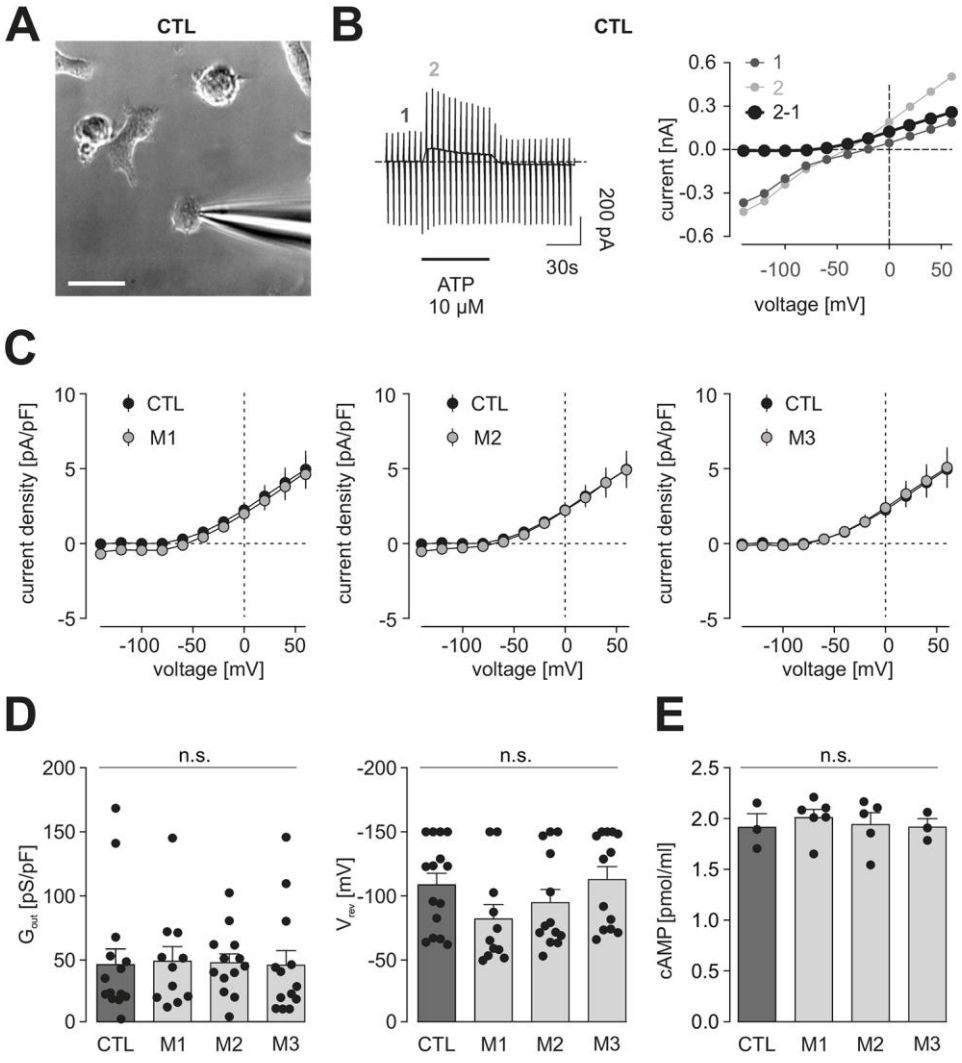

Fig. 4. Metabotropic purinergic responses are similar in CTL and *NF1*-mutant hiMGL cells

A Representative transmission light microscopy image of CTL hiMGL cells with the patch pipette approaching the cell. Scale bar: 20µm.

B Representative patch clamp experiments on CTL hiMGL cells. *Left*, Membrane currents are recorded from a single CTL hiMGL cell. The membrane was repetitively clamped at potentials between -140 and +60 mV every 5 s from a holding potential of -20 mV. Application of 10 µM ATP is indicated by the bar. Note the typical microglial response to ATP with activation of currents in the outward direction. *Right*, current-voltage relationships were obtained from the current recordings on the left. Purinergic responses (thick black) were determined by subtraction of I-V relations before (dark gray, 1) and during the first 15 s of ATP application (light gray, 2).

C Average current density to voltage relationships of ATP-induced metabotropic purinergic responses in microglia derived from CTL (black) and M1 (left), M2 (middle) or M3 (right) *NF1*-mutant iMGL cells.

D Summary of the outward conductance ($G_{ou}t$) between +20 mV and +60 mV (left) and the reversal potentials (V_{rev}) (right) of ATP (10 µM)-evoked currents from CTL and *NF1*-mutant hiMGL cells.

E cAMP levels of cell lysates from CTL and *NF1*-mutant hiMGL cells were measured by ELISA (n=3-6). For statistical analysis, 1-way ANOVA was performed.

Data in **C** and **D** are presented as the mean ± SEM, statistical comparison in **D** was done by a 1-way ANOVA test. Significance is indicated as followed: n.s., $p \geq 0.05$. Number of experiments: CTL=15, M1=11, M2=13, M3=13.

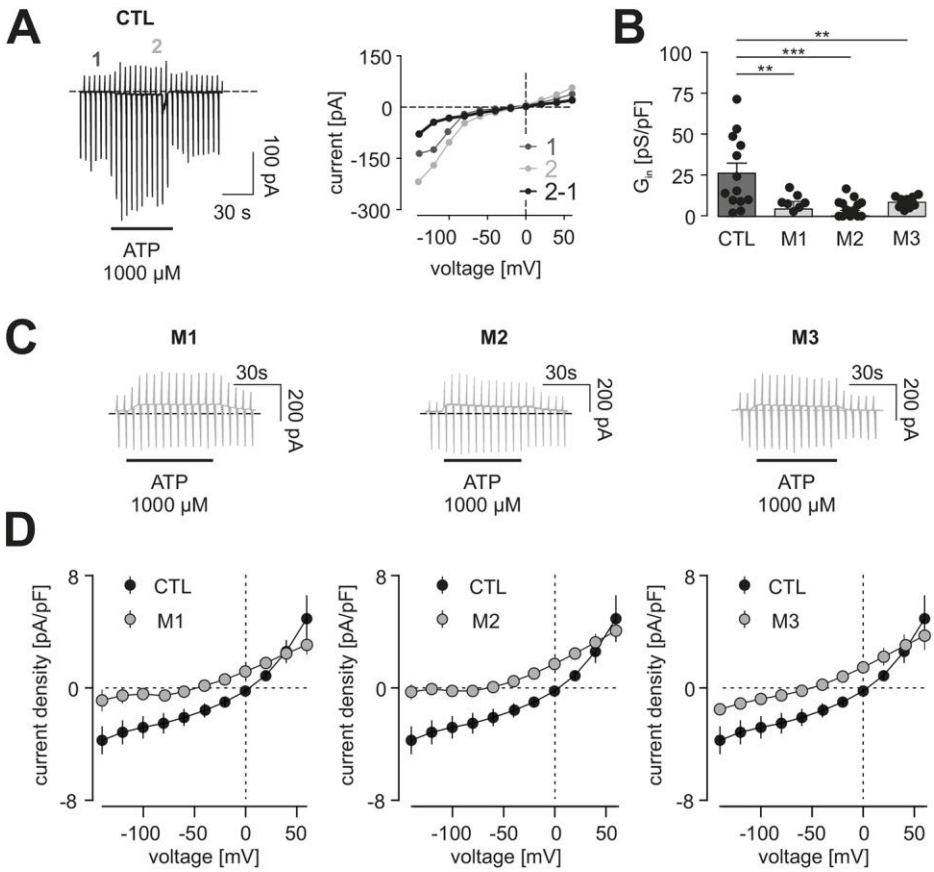

Fig. 5. Ionotropic purinergic responses are reduced in *NF1*-mutant hiMGL cells

A Representative patch clamp experiment. *Left*, Membrane currents recorded from a single CTL hiMGL cell. From a holding potential of -20 mV, membrane was repetitively clamped at potentials between -140 and +60 mV every 5s. Application of 1000 µM ATP is indicated by the bar. Please note the typical microglial response to ATP with activation of currents in inward- and outward directions. *Right*, current-voltage relationships obtained from the recording at the left. The purinergic response (thick black) was determined by subtraction of I-V relations before (dark gray, 1) and 15s after the onset of ATP application (light gray, 2).

B Summary of the inward conductance of ATP (1000 µM) – evoked currents between -100 mV and -120 mV.

C: Sample time courses currents clamped at potentials as described in A of M1 (left), M2 (middle) and M3 (right) hiMGL cells during application of 1000 µM ATP as indicated by bar. Note the absence of evoked inward currents.

D: Average current density to voltage relationships of ATP-induced (1000 µM) purinergic responses in CTL hiMGL cells relative to the three *NF1*-mutant hiMGL cell lines.

Data in **B** and **D** are presented as the mean ± SEM, statistical comparison in **B** was performed using a one-way ANOVA followed by a Dunnett's multiple comparisons test. Significance is indicated as followed: n.s., $p \geq 0.05$**, $p \leq 0.01$, ***, $p \leq 0.001$. Number of experiments: CTL=13, M1=9, M2=14, M3=11.

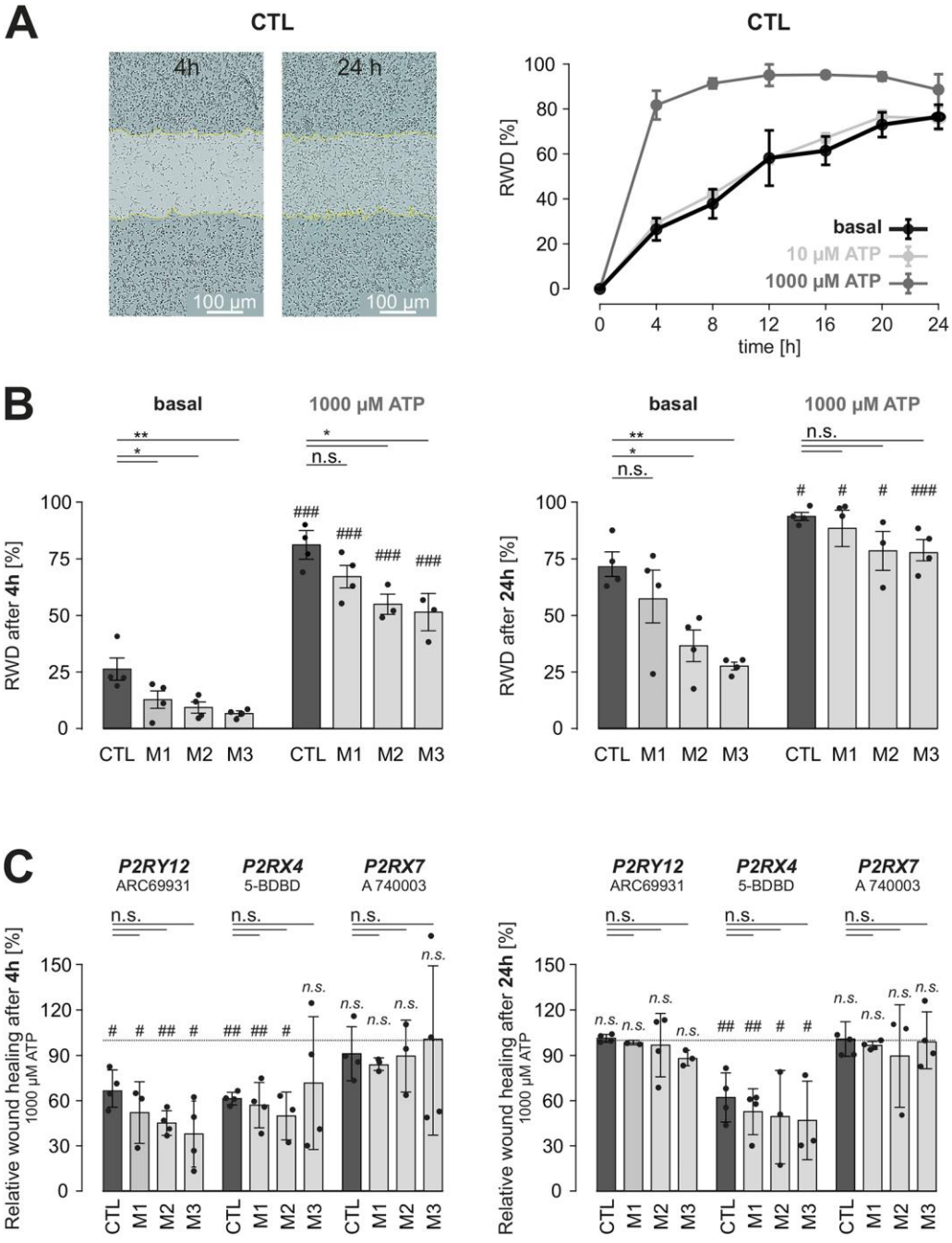

Fig. 6. Basal and ATP-induced motility in CTL and *NF1*-mutant hiMGL cells

A: *Left*, Representative images from CTL hiMGL cells scratch wound experiments analyzed at 4h and 24h after initial wound making. Color masks (white) and dotted lines (yellow) indicate the initial scratch wound area and border, respectively at 0h. Scale bar: 100 µm. *Right*, Relative Wound Density (RWD) was assessed over the course of 24h comparing CTL hiMGL cell motility in the absence and presence of ATP (10 µM and 1000 µM).

B: RWD under control conditions and in the presence of 1000 µM ATP after 4h (*left*) and 24h (*right*) represented as mean ± SEM. N = 4 for CTL and *NF1*-mutants. Data indicated by asterisks were analyzed by one-way ANOVA followed by Tukey's multiple comparisons test. N.S.; P>0.05;

*P<0.05; **P< 0.01. Comparisons between basal and 1000 µM ATP conditions were performed using a Student's t-test: #P<0.05; ###P<0.001.

C: RWD in the presence of 1000 µM ATP and inhibitors of either P2RY12 (10 µM ARC69931), P2RX4 (100 µM 5-BDBD), or P2RX7 (100 µM A 740003). Data are normalized to the RWD values for CTL or mutant hiMGL cells in the absence of inhibitors (1000 µM ATP only).

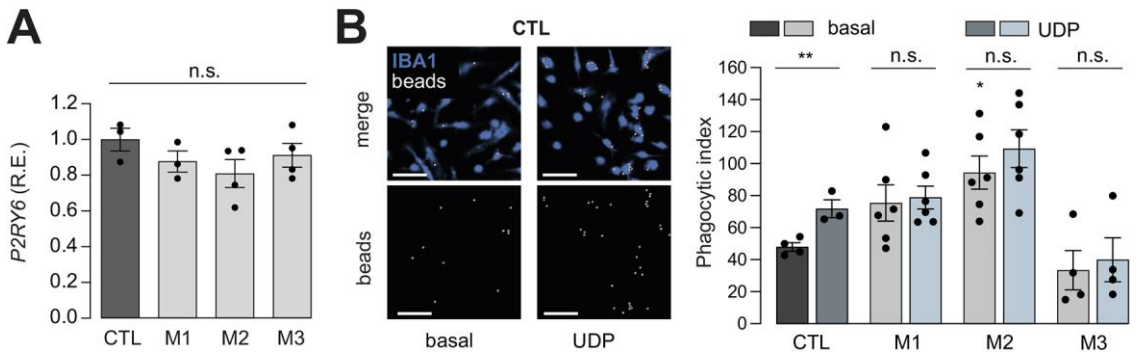

Fig. 7. Analysis of differences in phagocytic activity between CTL and *NF1*-mutant hiMGL cells

A Relative *P2RY6* mRNA expression levels in CTL and *NF1*-mutant hiMGL cells by quantitative RT-PCR. Relative expression (R.E.) is shown relative to CTL hiMGL cells. TATA box binding protein (*TBP*) was used as a housekeeping gene for normalization (n = 3). Data were the normalized to *P2RY6* expression in CTL hiMGL cells. Results are represented as the mean ± SD. Data were analyzed using a one-way ANOVA.

B Phagocytic activity was assessed using fluorescent microbeads. CTL and *NF1*-mutant hiMGL cells were incubated for 1 h with the beads with or without the addition of 100 µM UDP. *Left,* Representative images of CTL hiMGL cells at the end of the assay under basal and UDP conditions. IBA1 staining is indicated in blue and the beads are indicated in white. Top panels are an overlay of IBA1 (blue) and beads (white), whereas the lower panels show beads only. Control and UDP (100 µm) conditions are shown in the left and right panels, respectively. Scale bars: 20 µm. *Right*: Phagocytic activity presented as a phagocytic index, which is a measure of the percentage of cells exhibiting 0, 1, 2 or >3 engulfed beads. Data indicated by asterisks were analyzed using a one-way ANOVA followed by Tukey's multiple comparisons test. *P<0.05; **P< 0.01, ***P<0.001. Comparisons between basal and UDP conditions were performed using a Student's t-test: #P<0.05. Results are represented as the mean ± SEM. N = 5 for CTL and N = 3 for *NF1*-mutant hiMGL cells. Outliers were identified using the Grubb's test and removed accordingly.

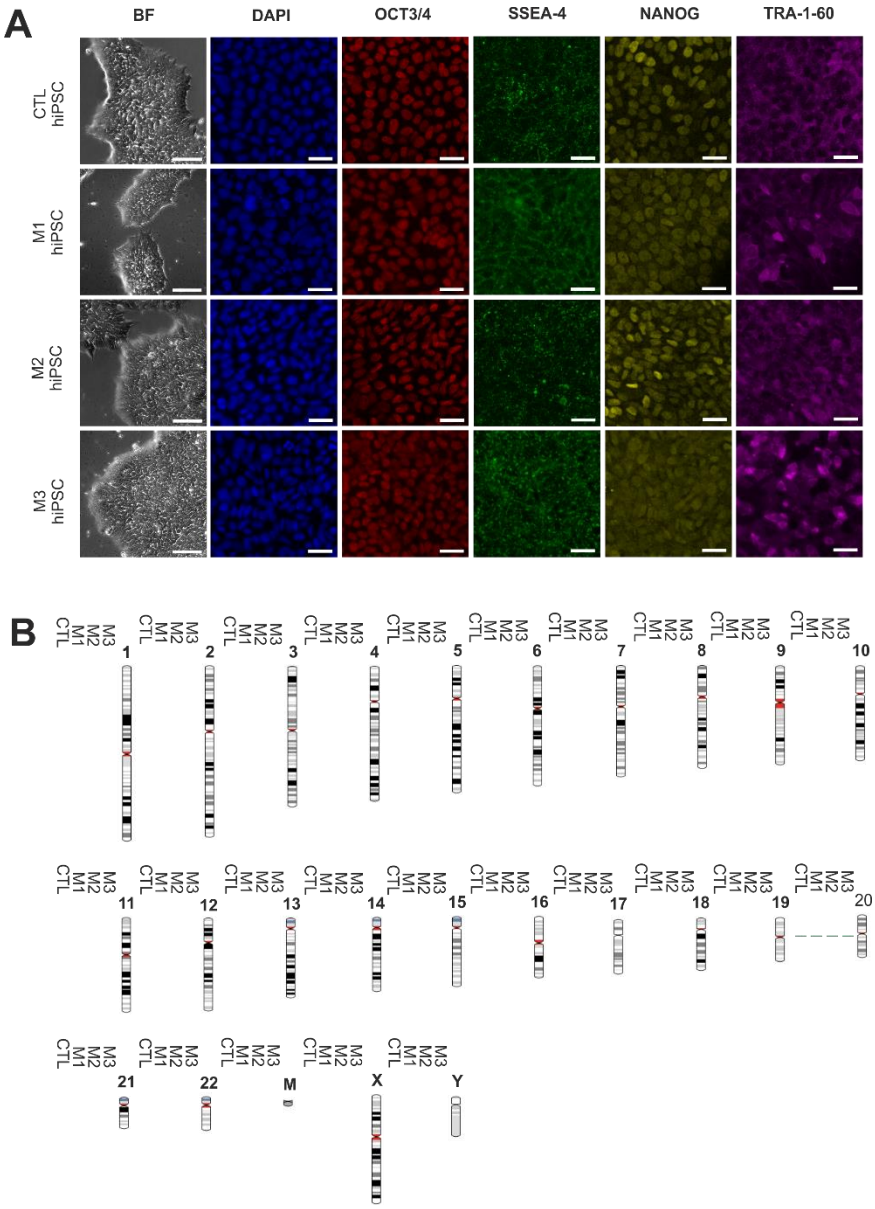

Fig. S1. Pluripotency immunocytochemistry and single nucleotide polymorphism (SNP)-karyotyping of CTL and *NF1*-mutant hiPSCs

A Brightfield (BF) images and immunocytochemical analysis of CTL and *NF1*-mutant hiPSC cells for OCT3/4, SSEA-4, NANOG and TRA-160 pluripotency markers. Scale bars, 100 μm (BF) and 30 μm.

B Virtual karyotype generated through SNP-karyotyping for all hiPSC lines. Areas of gain are marked in green, areas of loss in red, and loss of heterozygosity in gray.

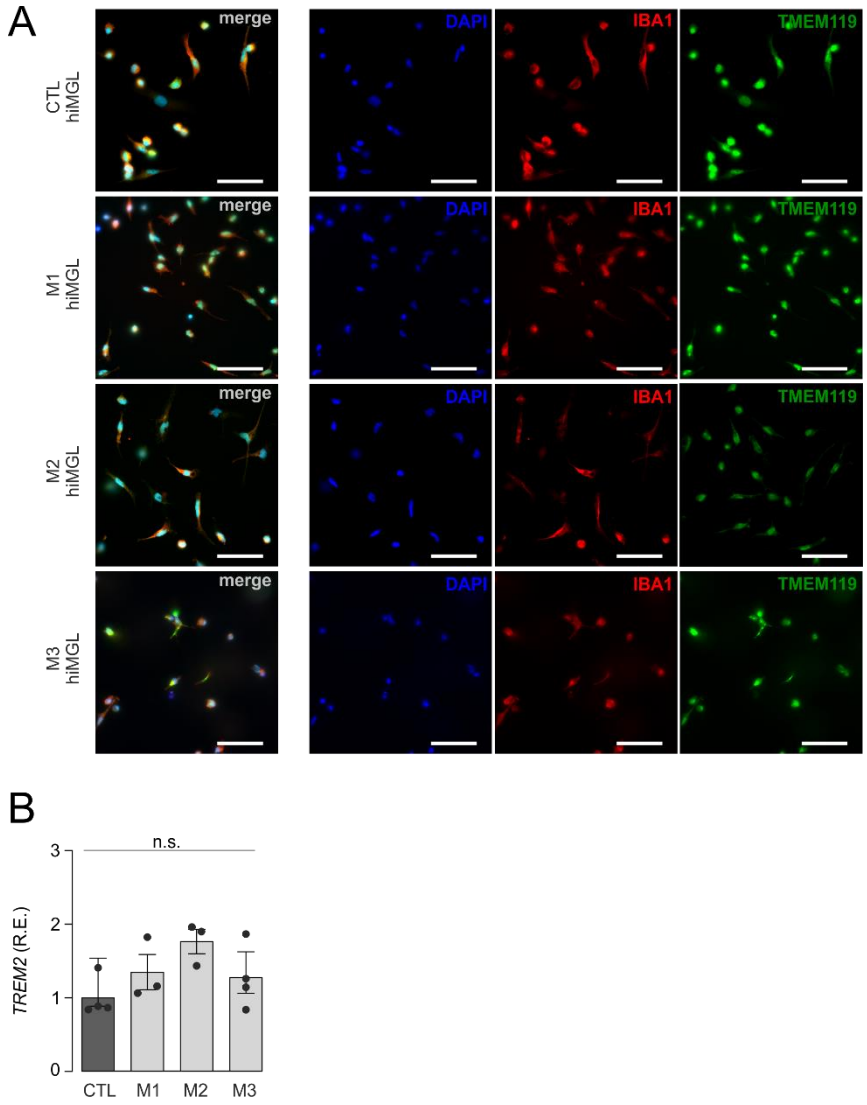

Fig. S2. Immunohistochemical staining and TREM2 expression in CTL and *NF1*-mutant hiMGL cells

A CTL and *NF1*-mutant hiMGL cells labelled with DAPI are immunopositive for IBA1 and TMEM119 expression. Merged images show the combined signal for DAPI, IBA1 and TMEM119. Scale bars, 50 µm.

B Relative mRNA expression levels of the *TREM2* microglia marker were assessed in CTL and *NF1*-mutant hiMGL cells by quantitative RT-qPCR. Relative expression (R.E.) was normalized relative to the TATA box binding protein (*TBP*) housekeeping gene (n=3). Results are represented as the mean ± SEM. Data were analyzed by one-way ANOVA followed by Tukey's multiple comparisons test.

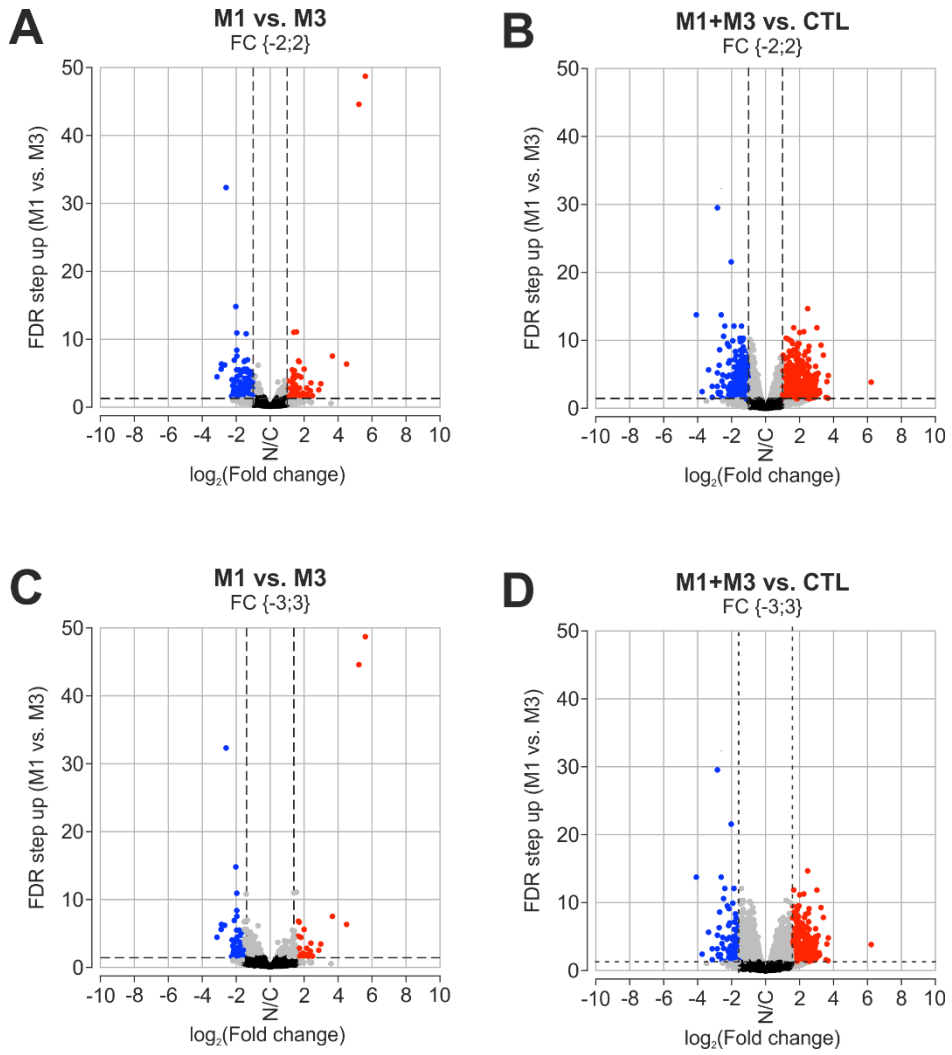

Fig. S3. RNAseq reveals few differences between NF1-mutant and CTL hiMGL cells

A Volcano plot demonstrating genes differentially expressed between M1 versus M3 [FDR < .05; fold change (-2, 2)]. Grey dots (no change), blue dots (decreased expression), red dots (increased expression).

B Volcano plot demonstrating genes differentially expressed between M1 versus M3 [FDR < .05; fold change (-3, 3)]. Grey dots (no change), blue dots (decreased expression), red dots (increased expression).

C Volcano plot demonstrating genes differentially expressed between M1 and M3 versus CTL [FDR < .05; fold change (-2, 2)]. Grey dots (no change), blue dots (decreased expression), red dots (increased expression).

D Volcano plot demonstrating genes differentially expressed between M1 and M3 versus CTL [FDR < .05; fold change (-3, 3)]. Grey dots (no change), blue dots (decreased expression), red dots (increased expression).

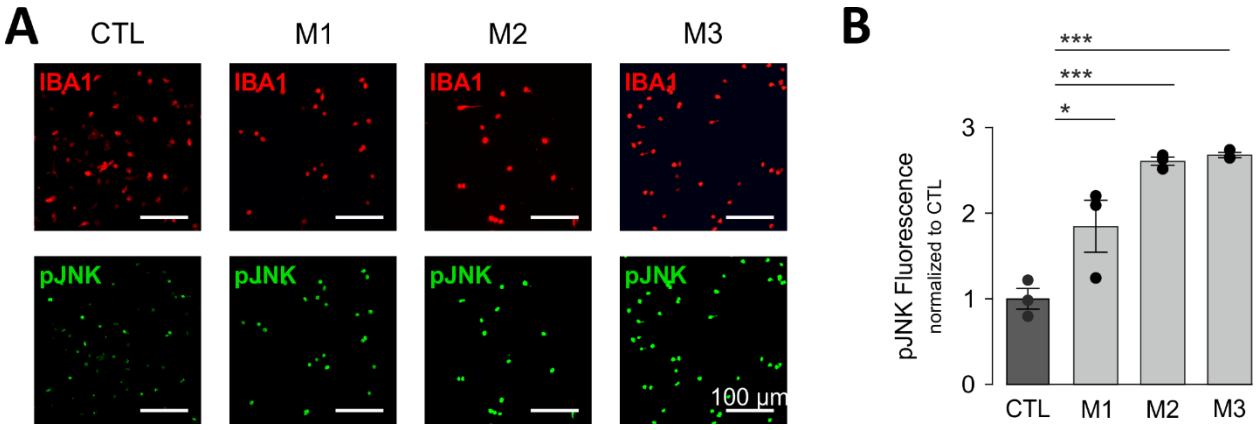

Fig. S4. *NF1*-mutant hiMGL cells show higher p-JNK expression than CTL hiMGL cells

A Immunohistochemical staining of CTL and *NF1*-mutant (M1-M3) hiMGL cells for IBA1 (red, *top*) and phosphorylated (activated) JNK (phospho-Thr^{183}/Tyr^{185} JNK, p-JNK; green, *bottom*). Scale bars, 100 µm.

B Quantification of phospho-JNK (p-JNK) fluorescence intensity in M1, M2 and M3 hiMGL cells, normalized to CTL hiMGL cells. Data indicated by asterisks were analyzed using a one-way ANOVA followed by Tukey's multiple comparisons test. *P<0.05; ***P<0.001. Results are represented as the mean +/- SEM. N = 3 independent differentiations for each mutant.

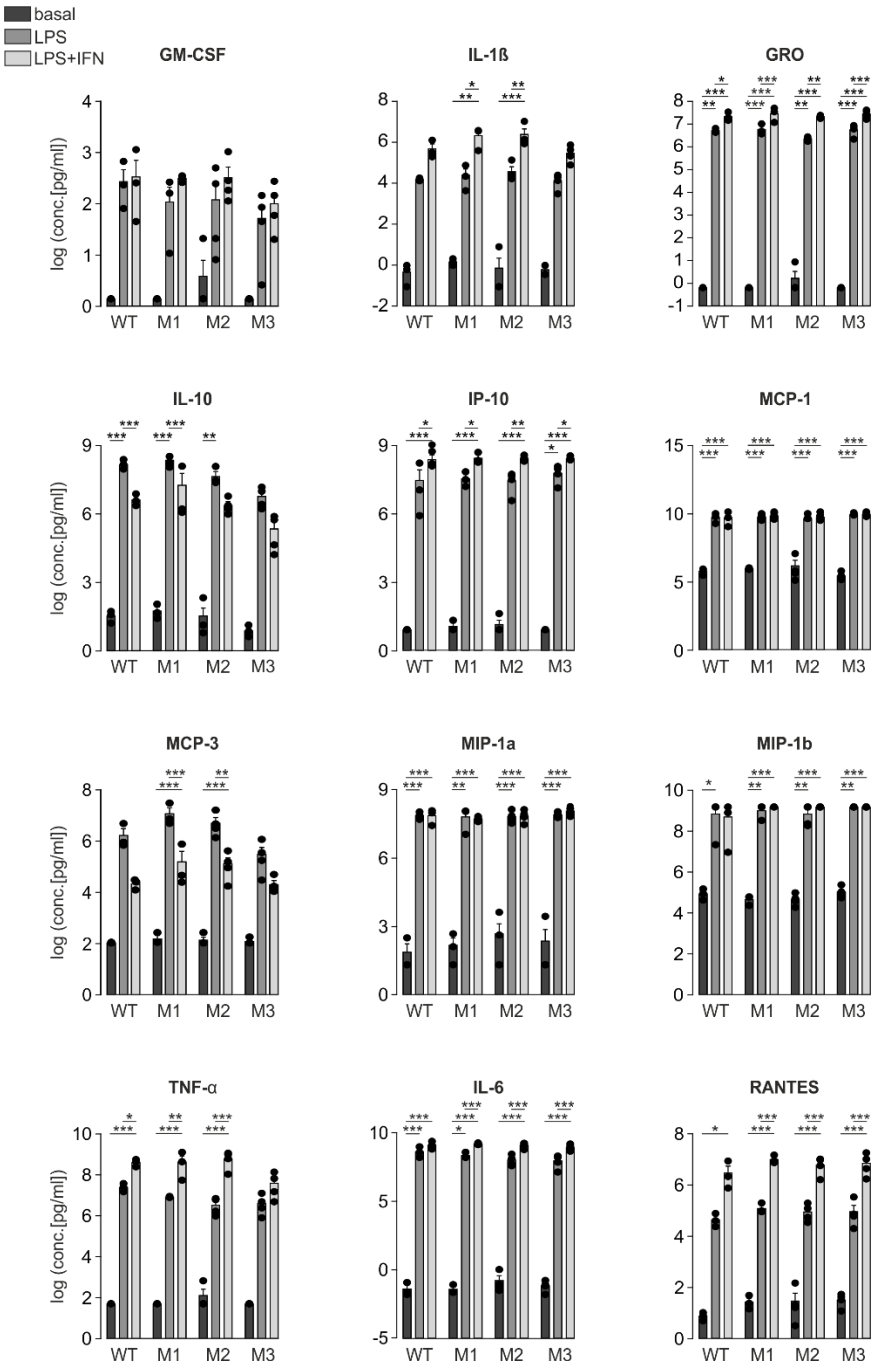

Fig. S5. Cytokine release from CTL and *NF1*-mutant hiMGL cells

A multiplex immunoassay was used to detect cytokines/chemokines secreted into the tissue culture medium by CTL and *NF1*-mutant hiMGL cells in response to stimulation with 1 µg/ml LPS or 1 µg/ml LPS + 100 ng/ml IFN-γ for 24h (n = 3-4). Data were analyzed by an ANOVA test. *P<0.05; **P< 0.01, ***P<0.001. Results are represented as the mean ± SEM.

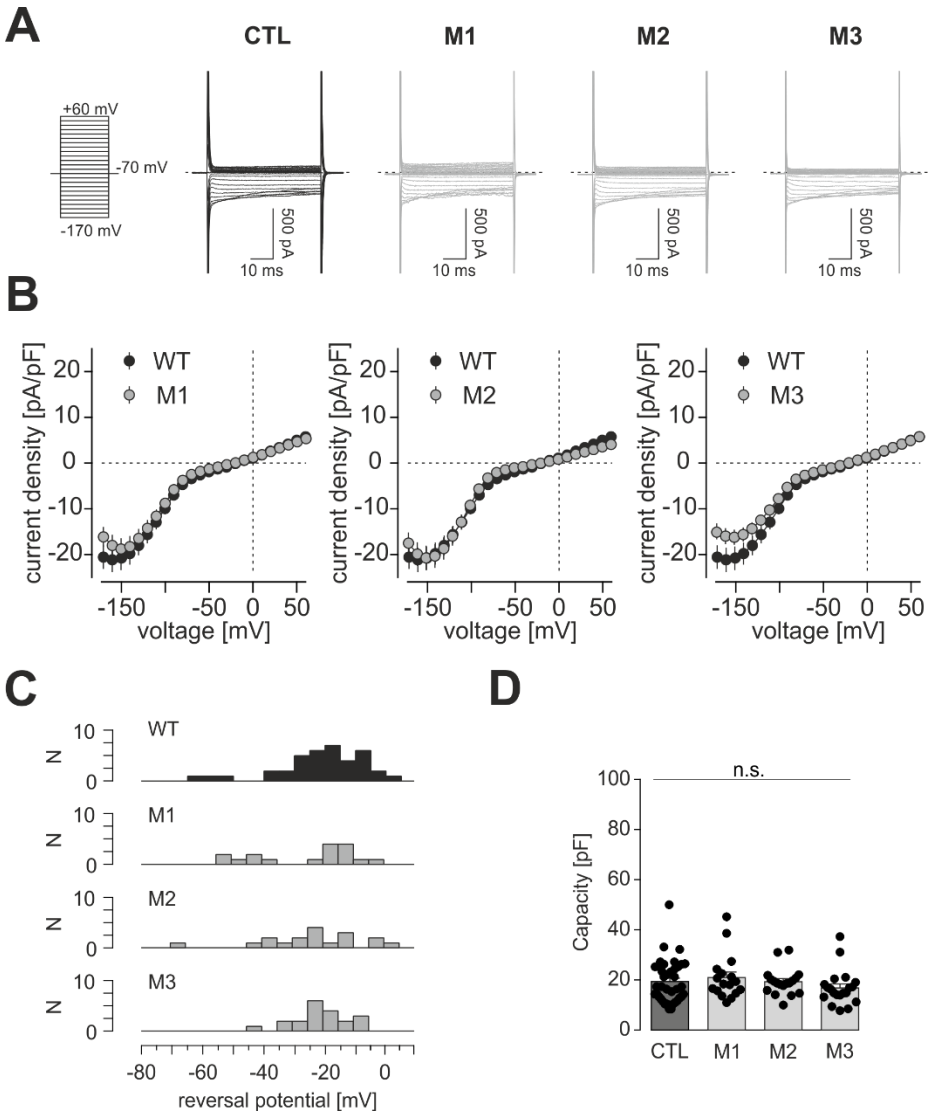

Fig. S6. Basal membrane properties of CTL and *NF1*-mutant hiMGL cells

A Sample patch clamp recordings of CTL and *NF1*-mutant hiMGL cells. Membrane currents were obtained during a series of voltage steps for 50 ms ranging from -170 mV to +60 mV from a holding potential of -70 mV.

B Average current density-voltage relationships of hiMGL cells obtained from the recordings shown in **A**.

C Distribution of the reversal potentials (indicative of the membrane potentials). N: number of patched cells.

D: Summary of the membrane capacities of CTL and *NF1*-mutant hiMGL cells.

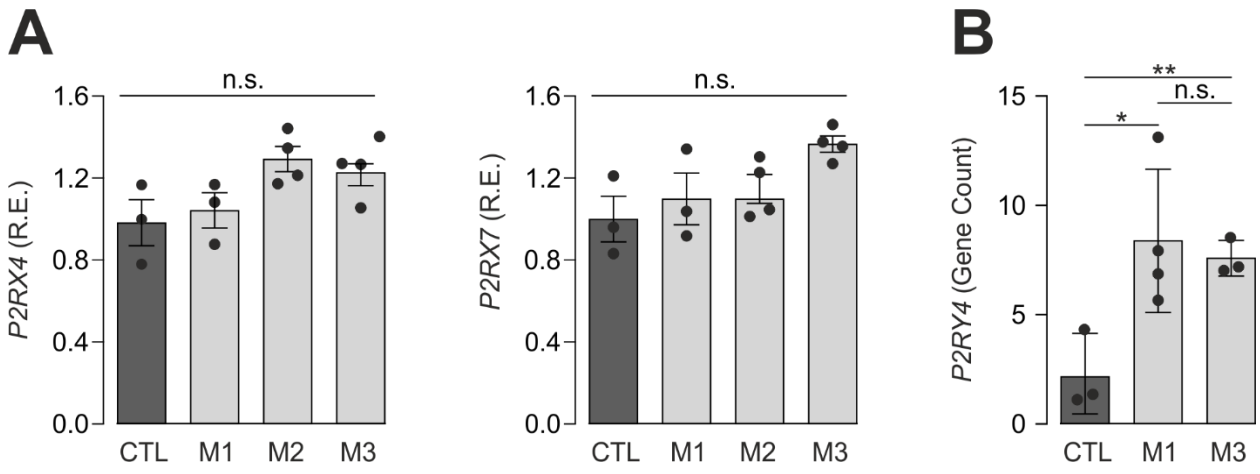

Fig. S7. Expression of P2RX4 and P2RX7 in CTL and *NF1*-mutant hiMGL cells

A: Relative *P2RX4* (left) and *P2RX7* mRNA expression (right) levels in CTL and *NF1*-mutant hiMGL cells by quantitative RT-PCR. TATA box binding protein (*TBP*) was used as a housekeeping gene for normalization (n = 3). Data were then normalized to mRNA expression levels in CTL hiMGL cells. Results are represented as the mean ± SD. Data were analyzed by one-way ANOVA.

B: P2 receptor expression from the RNA sequencing data revealed that only *P2RY4* expression was different in *NF1*-mutant hiMGL cells relative to CTL hiMGL cells. P values are included in the graph. All other genes were not statistically different between *NF1*-mutant and CTL hiMGL cell groups.

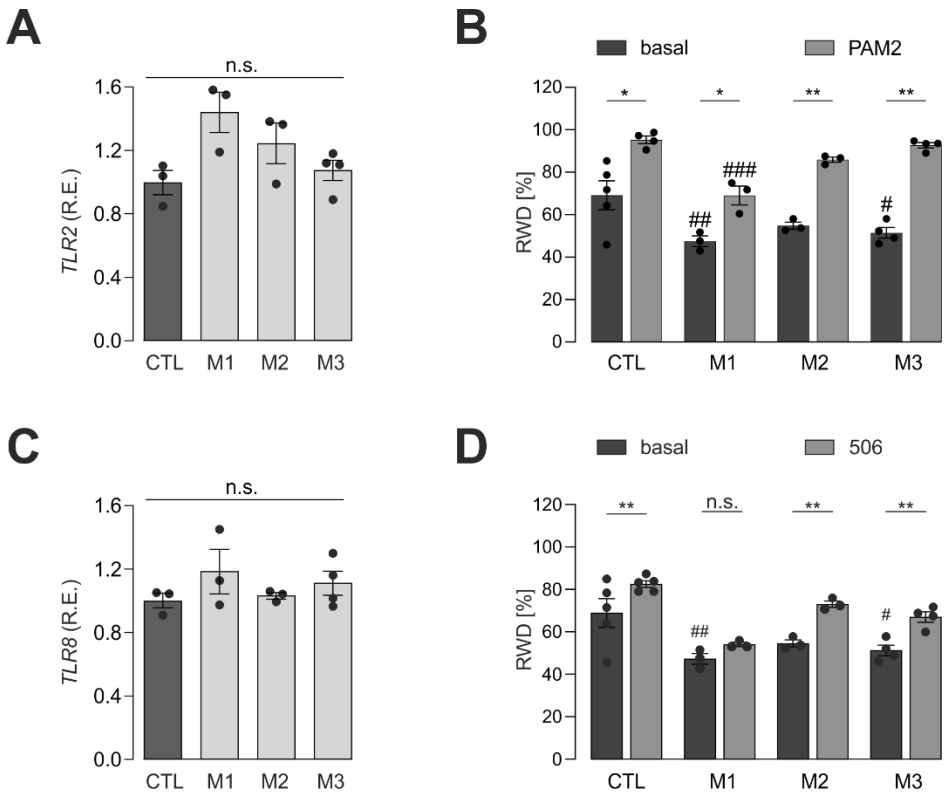

Fig. S8. Motility of CTL and *NF1*-mutant hiMGL cells

A Relative mRNA expression levels of Toll-like receptor 2 (*TLR2*) in CTL and *NF1*-mutant hiMGL cells by quantitative RT-PCR. Relative expression (R.E.) is shown relative to CTL hiMGL cells. TATA box binding protein (*TBP*) mRNA expression was used as a housekeeping gene for normalization (n = 3). Data were then normalized to *TLR2* expression of CTL hiMGL cells. Results are represented as the mean ± SEM. Data were analyzed by one-way ANOVA.

B Motility was assessed using a standardized wound scratch assay (RWD) using an Incucyte Zoom System. hiMGL cells were incubated with or without Pam2CSK4 (100 ng/ml). Relative Wound Density (RWD) was assessed over the course of two days comparing CTL and *NF1*-mutant hiMGL cells. Results are represented as the mean ± SEM. N = 5 for CTL and N = 3-4 for *NF1*-mutant hiMGL cells. Data indicated by the asterisks were analyzed by one-way ANOVA followed by Tukey's multiple comparisons test. *P<0.05; **P< 0.01, ***P<0.001. Comparisons between basal and Pam2CSK4 conditions were performed using a Student's t-test: #P<0.05, ###P<0.001.

C Relative mRNA expression levels of Toll-like receptor 8 (*TLR8*) was assessed in CTL and *NF1*-mutant hiMGL cells by quantitative RT-PCR. TATA box binding protein (*TBP*) was used as a housekeeping gene for normalization (n=3). Data were then normalized to *TLR8* expression of CTL hiMGL cells. Results are represented as the mean ± SD. Data were analyzed by one-way ANOVA.

D RWD after 36h was represented as the mean ± SEM. N = 5 for CTL and N = 3 for *NF1*-mutant hiMGL cells. hiMGL cells were incubated with or without 506 (100 ng/ml). Data indicated by the asterisks were analyzed by one-way ANOVA followed by Tukey's multiple comparisons test. *P<0.05; **P< 0.01, ***P<0.001. Comparisons between basal and 506 conditions were performed using a Student's t-test: ##P<0.01.

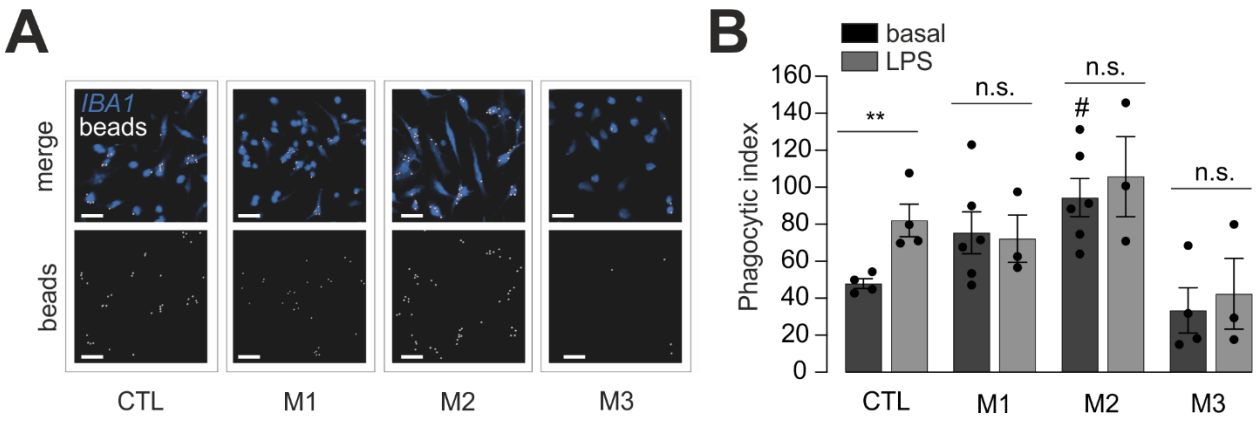

Fig. S9. Phagocytic activity of CTL and *NF1*-mutant hiMGL cells

Phagocytic activity was assessed by microscopy using fluorescent microbeads. CTL and *NF1*-mutant hiMGL cells were incubated for 1h with beads with or without addition of 1 µg/ml LPS.

A: Representative images of CTL and *NF1*-mutant hiMGL cells at the end of the assay period under LPS stimulation conditions. IBA1 staining is indicated in blue and beads in white. Scale bars, 20 µm.

B: Phagocytic activity presented as the phagocytic index, which is a measure of the percentage of cells harboring 0, 1, 2 or >3 engulfed beads. Data indicated by asterisks were analyzed by one-way ANOVA followed by Tukey's multiple comparisons test. *P<0.05; **P< 0.01, ***P<0.001. Comparisons between basal and UDP conditions were performed using a Student's t-test: ###P<0.001. Results are represented as the mean ± SEM. N = 5 for CTL and n = 3 for *NF1*-mutant hiMGL cells.

Table S1. Antibodies used

Antibody	Company	Host species	Dilution	Catalog number
Anti-IBA1	Abcam	Goat	1:250	ab5076
Anti-NANOG	Thermo Fisher Scientific	Rabbit	1:100	PA1-097
Anti Phospho-JNK (phospho-T183/Y185)	R&D Systems	Rabbit	1:100	MAB1205
Anti-OCT-3/4	Santa Cruz	Rabbit	1:100	sc-9081
Anti-P2RY12	Genetex	Rabbit	1:200	GTX54796
Anti-SSEA-4	Abcam	Mouse	1:100	ab16287
Anti-TMEM119	Abcam	Rabbit	1:200	ab185333
Anti-TRA-1-60	Abcam	Mouse	1:100	ab16288

Table S2. Primers used

Primer		Sequence
AIF1	forward	5’- TTGGTGAGAAACGGGTGATTTG-3’
	reverse	5’- ATGGAGCATGTAGGAGAGACC-3’
P2RX4	forward	5’- GAGATTCCAGATGCGACCACT-3’
	reverse	5’- ACCCGTTGAAAGCTACGCAC-3’
P2RX7	forward	5’- TATGAGACGAACAAAGTCACTCG-3’
	reverse	5’- GCAAAGCAAACGTAGGAAAAGAT-3’
P2RY6	forward	5’- GTGTCTACCGCGAGAACTTCA-3’
	reverse	5’- CCAGAGCAAGGTTTAGGGTGTA-3’
P2RY12	forward	5’- CACTGCTCTACACTGTCCTGT-3’
	reverse	5’- AGTGGTCCTGTTCCCAGTTTG-3’
TBP1	forward	5’- AGCGCAAGGGTTTCTGGTTT-3’
	reverse	5’- CTGAATAGGCTGTGGGGTCA-3’
TLR2	forward	5’- TTATCCAGCACACGAATACACAG-3’
	reverse	5’- AGGCATCTGGTAGAGTCATCAA-3’
TLR4	forward	5’- TGGAAGTTGAACGAATGGAATGTG-3’
	reverse	5’- ACCAGAACTGCTACAACAGATACT-3’
TLR8	forward	5’- CCACCTTGAAGAGAGCCGAG-3’
	reverse	5’- TGCTCTGCATGAGGTTGTCG-3’
TMEM119	forward	5’- GAGGAGGGACGGGAGGAG-3’
	reverse	5’- CAGAAGGATGAGGAGGCTGG-3’

Table S3. Differentially expressed genes between M1 & M3 relative to CTL hiMGL cells

Gene name	P-value	FDR	Fold change (M1 & M3 vs. CTL)
DCANP1	6.18E-06	1.82E-04	71.76
GPR22	2.13E-05	4.53E-04	15.36
FOXN3-AS2	3.54E-10	1.07E-07	12.56
EHF	7.92E-05	1.18E-03	9.39
SAA1	7.42E-04	6.31E-03	9.31
YY1P1	5.45E-12	3.98E-09	9.00
RNF43	3.96E-03	2.18E-02	8.81
KCNAB1	2.76E-06	1.00E-04	7.57
ZNF22-AS1	2.83E-05	5.54E-04	7.44
CDH1	8.37E-04	6.93E-03	7.18
DSP	7.36E-05	1.12E-03	7.01
FAM83B	1.49E-03	1.06E-02	6.99
TAS2R30	5.23E-05	8.71E-04	6.65
OR7E38P	7.98E-06	2.17E-04	6.56
GAS8	6.93E-03	3.28E-02	6.54
KLB	2.36E-03	1.47E-02	6.36
OGN	1.29E-07	1.00E-05	6.32
EIF1P7	7.56E-03	3.51E-02	6.11
PLGLB2	6.39E-07	3.33E-05	6.02
LBH	1.08E-03	8.39E-03	5.95
PLN	2.00E-05	4.35E-04	5.94
LAMP3	9.26E-04	7.43E-03	5.90
PRMT5-AS1	7.23E-04	6.20E-03	5.76
SRGAP2-AS1	1.77E-05	3.99E-04	5.70
GNPDA2	3.21E-07	1.97E-05	5.45
PIGAP1	1.63E-06	6.66E-05	5.23
TAS2R13	4.79E-05	8.22E-04	5.22
DIAPH1-AS1	4.10E-09	7.42E-07	5.21
HSBP1L1	7.00E-03	3.30E-02	5.18
CCL22	7.69E-05	1.16E-03	5.18
CTXND1	8.63E-03	3.87E-02	5.16
CD1A	1.19E-08	1.68E-06	5.16
ATP5PDP4	2.24E-06	8.42E-05	5.13
TAS2R31	5.12E-04	4.81E-03	5.12
OR10A2	6.28E-04	5.59E-03	5.09
MANEA-DT	5.40E-03	2.72E-02	5.08
HSPD1P11	1.56E-03	1.09E-02	5.02
TMEM178A	1.61E-03	1.12E-02	-5.20
SAP25	2.52E-18	9.56E-15	-5.28
DNAH8	3.41E-04	3.57E-03	-5.39
PDCD6-AHRR	1.73E-14	4.11E-11	-5.80

TNFSF9	3.42E-06	1.18E-04	-5.94
SYNPO2L-AS1	6.61E-08	6.03E-06	-5.94
CAT	1.70E-20	1.08E-16	-6.39
DNAAF4-CCPG1	6.59E-06	1.90E-04	-6.39
GOPC	7.45E-27	1.21E-22	-6.90
MUSTN1	5.03E-04	4.77E-03	-7.80
CEMP1	7.07E-07	3.59E-05	-8.05
SDHAP2	6.63E-13	7.51E-10	-15.60

Table S4. Differentially expressed genes between M1 vs. M3 hiMGL cells

Gene name	P-value	FDR	Fold change (M1 vs. M3)
GOPC	7.08E-40	1.35E-35	46.33
ZNF252P	2.21E-33	2.10E-29	30.69
DNAAF4-CCPG1	6.18E-05	1.07E-02	10.40
MIR124-1HG	2.11E-04	2.39E-02	5.18
PCDHA10	3.09E-04	3.14E-02	5.04
BIRC3	2.29E-04	2.50E-02	-5.08
LTBP1	2.67E-08	2.21E-05	-5.96
PCDHGA10	1.66E-28	1.05E-24	-6.03
PRSS8	2.14E-09	2.55E-06	-6.69
TSSC2	4.48E-05	8.60E-03	-9.57
EHF	3.19E-11	5.05E-08	-11.10

Table S5. Materials for cell culture and *in vitro* experiments

Product name	Company	Catalog number
α-Thioglycerol	Merck	M1753-100ML
24-well plates	Sarstedt	83.3922
4′,6-diamidino-2-phenylindole (DAPI)	Merck	32670
Aqua-Poly/Mount	Polysciences Europe GmbH	18606
B-27 Supplement (50X), serum free	Life Technologies	17504-044
Bambanker	GC Lymphotec	302-14681
CD200, Human 50µg	Novoprotein	C311
CX3CL1, 5µg	Peprotech	300-31
Cyclic CAMP ELISA Kit	Cayman Chemical	581001
DMEM/F-12, HEPES, no phenol red	Life Technologies	11039-021
Donkey serum	Merck	S30
Falcon® 6-well Clear Flat Bottom Plates	Corning	353046
Fetal Calf Serum (FCS)	Life Technologies	10270-106
Fluoresbrite® YG Carboxylate Microspheres, 3.00µm	Polysciences Europe GmbH	17147-5
Geltrex™	Life Technologies	A14133-02
GlutaMAX Supplement-100 mL	Life Technologies	35050-038
HBSS	Life Technologies	14175-129
Human Insulin	PromoCell	C-52310
IL-34 2µg	Peprotech	200-34
Incucyte® Imagelock 96-well plates	Sartorius	BA-04856
Insulin-Transferrin-Selenite	Life Technologies	41400-045
Lipopolysaccharide from *E.coli*	Merck	L43191

M-CSF	Peprotech	300-25
MEM Non-Essential Amino Acids Solution (100X)-100 mL	Life Technologies	11140-035
N-2 Supplement (100X)	Life Technologies	17502-048
PBS	Life Technologies	14190-169
ReliaPrep™ RNA Tissue Kit	Promega	Z6112
STEMdiff™ Hematopoietic Kit	Stemcell Technologies	5310
StemMACS™ iPS-Brew XF	Miltenyi Biotec	130-107-086
StemPro® Accutase®	Life Technologies	A11105-01
SYBR Green Master Mix	Life Technologies	4472918
TGFβ1	Peprotech	100-21C
Thiazovivin	StemCell Technologies™	72252
Triton® X-100	Roth	3051.3